Journal of Materials Research and Technology 39 (2025) 8602–8618

Contents lists available at ScienceDirect

Journal of Materials Research and Technology

journal homepage: www.elsevier.com/locate/jmrt

Tailoring the mechanical properties of the multicomponent lightweight alloy $Al_{58}Zn_{28}Mg_6Si_8$ via composition and processing-route engineering

J.J. Trujillo-Tadeo [a,b,*], J. Victoria-Hernández [a], P. Garcia-Michelena [b], P. Jimbert [c], C. Hartmann [d], D. Letzig [a], I. Hurtado [b], G. Arruebarrena [b]

[a] Institute of Material and Process Design, Helmholtz-Zentrum Hereon, Max-Planck-Str. 1, Geesthacht, D-21502, Germany
[b] Mechanical and Manufacturing Department, Faculty of Engineering, Mondragon Unibertsitatea, Arrasate/Mondragon, 20500, Spain
[c] Bilbao School of Engineering, University of the Basque Country UPV/EHU, 48013, Bilbao, Spain
[d] Technical University of Munich, Chair of Metal Forming and Casting, Walther-Meissner-Strasse 4, Garching, 85748, Germany

ARTICLE INFO

Keywords:
Multicomponent alloy
Lightweight alloy
Directional solidification
Near solidus forming

ABSTRACT

In this study, the multicomponent (medium entropy) lightweight alloy $Al_{58}Zn_{28}Mg_6Si_8$ was systematically improved through a dual optimization strategy. First, the chemical composition was adjusted using the CALPHAD methodology, reducing the Si content and incorporating Sr and Sb as modifying elements to control intermetallic phase formation.

This optimization led to the new composition $Al_{60}Zn_{27}Mg_{11}Si_2$, effectively suppressing the formation of primary Si and altering the morphology of the Mg_2Si phase. Second, the alloy microstructure was modified using two processing techniques—Directional Solidification (DS) and Near-Solidus Forming (NSF)—followed by heat treatment. These methods were selected to refine the microstructure, improve phase distribution, and enhance mechanical performance. Microstructural characterization and mechanical testing, including uniaxial compression and nanoindentation, were performed on both as-cast and heat-treated samples.

The results revealed that the combination of chemical and microstructure optimization significantly enhanced the compressive strength, increasing from 471 MPa to 769 MPa—a 61 % improvement. Additionally, directional solidification produced the finest lamellar-dendritic microstructure, resulting in the highest yield strength. However, the alloy remained brittle, with limited ductility despite structural refinement.

Overall, this work highlights the strong interdependence between composition, processing, and microstructure in determining the mechanical performance of multicomponent lightweight alloys. The findings provide a pathway for designing high-strength multicomponent systems tailored for structural applications.

1. Introduction

Enhancing fuel efficiency in aerospace and automotive applications continues to drive the development of advanced lightweight materials [1–4]. Multicomponent alloys—also referred to as high- or medium-entropy alloys, or complex concentrated alloys—generally explore the central region of multicomponent composition space and are composed of diverse elements in substantial atomic fractions. Owing to their remarkable properties, they have become a focal point of research interest [5–7]. Although alloy design strategies are well established for conventional binary/ternary Al–Mg–Zn–Si systems, systematic guidance becomes sparse when compositions move toward the center of multicomponent phase space, where higher solute contents and multi-solute interactions complicate phase stability, precipitation, and processing windows. This motivates the present study.

In Al-based systems with a dominant Al (FCC) solid solution, several alloying additions are known to tailor microstructure and mechanical response. Cu shifts precipitation toward θ' (Al_2Cu), S' (Al_2CuMg), and Q'-type phases, increasing yield strength and hardness; however, coarse/continuous Cu-rich intermetallics (Al_2Cu, Al_2CuMg) can localize strain and impair ductility and corrosion resistance [8,9]. In the melt, Cu also modifies fluidity/viscosity near the liquidus, affecting feeding and

---

[*] Corresponding author. Institute of Material and Process Design, Helmholtz-Zentrum Hereon, Max-Planck-Str. 1, Geesthacht, D-21502, Germany.

E-mail addresses: Juan-Jose.Trujillo-Tadeo@hereon.de (J.J. Trujillo-Tadeo), jose.victoria-hernandez@hereon.de (J. Victoria-Hernández), pgarciam@mondragon.edu (P. Garcia-Michelena), pello.jimbert@ehu.eus (P. Jimbert), christoph.hartmann@utg.de (C. Hartmann), dietmar.letzig@hereon.de (D. Letzig), ihurtado@mondragon.edu (I. Hurtado), garruebarrena@mondragon.edu (G. Arruebarrena).

https://doi.org/10.1016/j.jmrt.2025.11.149
Received 7 October 2025; Received in revised form 12 November 2025; Accepted 17 November 2025

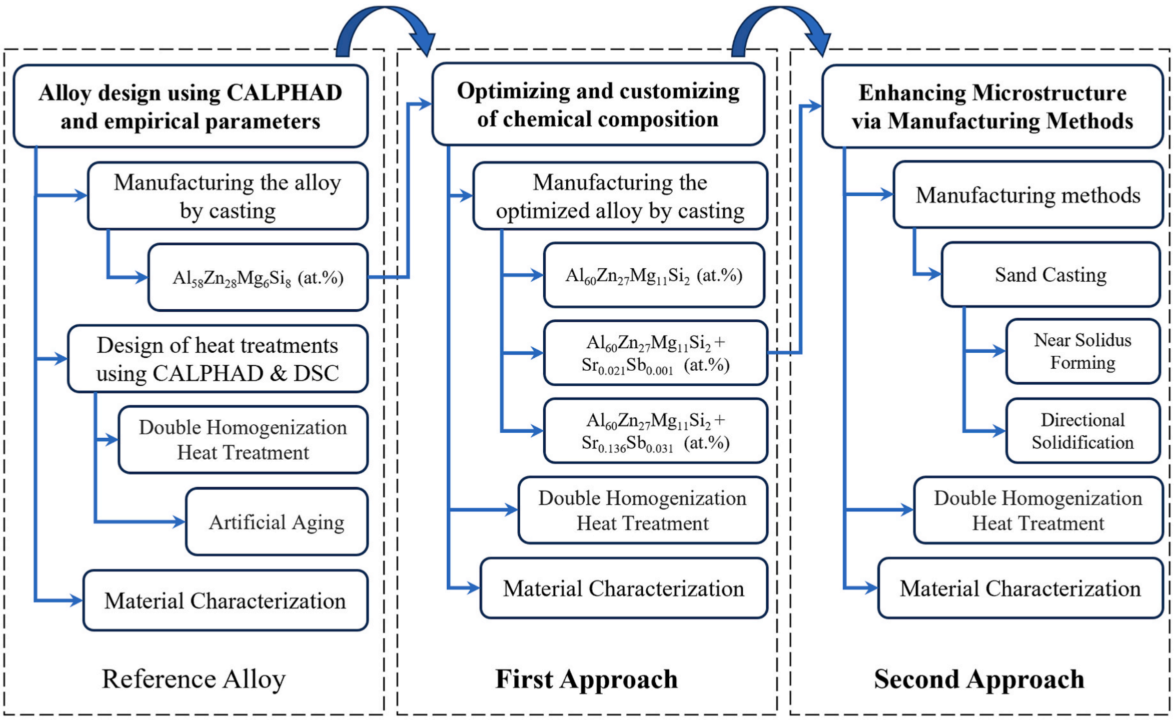

Fig. 1. Schematic of the three-part workflow: reference alloy (taken from previous work [20]), first approach "Optimizing and customizing chemical composition" — and second approach "Enhancing microstructure via manufacturing methods".

porosity, so strength gains must be balanced against castability [9]. In Al–Mg–Si alloys, Mg and Si control the $\beta'' \rightarrow \beta' \rightarrow \beta$ sequence, while Zn synergizes with Mg to stabilize η/η' ($MgZn_2$) and mixed Q-type precipitates, increasing hardenability but raising sensitivity to over-ageing and environment-assisted cracking [10,11]. The addition of Si can enhance melt flowability and castability, benefiting both casting and extrusion operations [12]. Moreover, sub-micron dispersoids formed with Zr, Cr, and Mn additions contribute to improved fracture toughness [13] and promote grain refinement [14]. Regarding Mn, prior studies report that Mn-containing dispersoids—such as Al_6Mn, $Al_{20}Cu_2Mn_3$, and $Al_{24}Mn_5Zn$ [15,16]—can increase yield strength and ultimate tensile strength [17], but may also reduce crack-growth resistance and degrade toughness [15]. Ti + B grain refiners ($TiB_2/TiAl_3$) reduce primary α-Al grain size and improve isotropy and feeding; re-precipitated TiB_2 routes have been explored to sustain refinement during processing [18,19]. However, most of this knowledge has been derived for alloys with a single dominant solid-solution matrix and limited second-phase volume fractions; its direct transfer to multicomponent, center-of-space compositions remains insufficiently validated.

The multicomponent alloy targeted here, $Al_{58}Zn_{28}Mg_6Si_8$ [20], exhibits a high Al (FCC) solid-solution fraction. Our design philosophy is to preserve this high solid solution and restrict compositional changes to the controlled modification of intermetallic phases, specifically (Si) and (Mg_2Si). Among strengthening constituents, Mg_2Si is particularly attractive due to its high melting point, low density, high hardness, low thermal expansion, and high elastic modulus; it is also non-toxic, corrosion-resistant, environmentally benign, and cost-effective [21]. A key challenge is that primary Mg_2Si tends to form coarse "Chinese-script" morphologies at slow solidification rates, introducing stress concentrators that degrade mechanical performance. Consequently, refining and modifying Mg_2Si is essential. Numerous studies report modification by Sb, Sr, Ca, Gd, Sc, Li, P, Y, and Ba, with Sr and Sb consistently delivering the most effective Mg_2Si modification [22–32]. Building on this evidence, we focus on combined Sr–Sb additions to refine/round Mg_2Si while keeping the Al (FCC) matrix highly supersaturated.

Processing is the second pillar of our approach. Conventional casting routes can suffer from inconsistency and defects (e.g., gas/shrinkage porosity), whereas advanced methods—high-pressure die casting, gravity casting, and squeeze casting—improve strength and microstructure but demand tight parameter control [33–37]. In parallel, Semi-Solid Metal (SSM) processing, by operating between solidus and liquidus, enhances plasticity and mechanical properties [7]. Within SSM, Near-Solidus Forming (NSF) achieves forging-like properties with lower energy and material usage, enabling complex geometries in a single deformation step just below the solidus [38–41]. Complementarily Conversely, Directional Solidification (DS) technology relies on a controlled cooling mechanism to establish a pronounced temperature gradient [42–45]. This enables molten metal to solidify in a specific direction, contrary to the heat flow [46,47]. This technique promotes the formation of fine, uniform microstructures that result in improved mechanical properties [43,48,49].

This work examines Sr–Sb co-modification of Mg_2Si in the $Al_{58}Zn_{28}Mg_6Si_8$ multicomponent system. We (i) study how Sr–Sb additions tailor Mg_2Si morphology while preserving a high Al (fcc) solid-solution fraction, and (ii) evaluate microstructural control by comparing NSF and DS processing. Our objective is to quantify the resulting microstructural evolution and mechanical properties and to identify an effective pathway that couples composition (Sr–Sb) and processing (NSF/DS) to maximize strength while maintaining defect tolerance and castability.

2. Materials and methods

The methodology employed in this investigation is illustrated in Fig. 1 below. The starting reference alloy for composition and microstructure optimization is the multicomponent lightweight alloy $Al_{58}Zn_{28}Mg_6Si_8$, as indicated in Ref. [20]. Various methods and techniques have been repeatedly employed for the characterization, mechanical properties measurement, and alloy fabrication throughout the study, with only occasional adjustments to measurement parameters.

Table 1
Chemical composition of the $Al_{60}Zn_{27}Mg_{11}Si_2$ multicomponent lightweight alloy and its Sr–Sb modified version, expressed in atomic percent (at.%) and weight percent (wt.%).

Alloy		Zn	Mg	Si	Sr	Sb	Al
Alloy 1	[wt.%]	47.20	7.15	1.23	–	–	Bal.
	[at.%]	26.68	10.87	1.64	–	–	Bal.
Alloy 2	[wt.%]	48.23	7.28	1.27	0.049	0.004	Bal.
	[at. %]	27.49	11.16	1.70	0.021	0.001	Bal.
Alloy 3	[wt.%]	47.70	6.92	1.28	0.320	0.100	Bal.
	[at.%]	27.19	10.62	1.70	0.136	0.031	Bal.

2.1. *Optimizing and customizing the chemical composition*

To optimize the chemical composition, the microstructure is being refined by reducing the silicon content and incorporating modifying elements, specifically strontium and antimony. The alloys were prepared by gravity die casting (DC), using Al, Zn, Mg, and Si of commercial purity as starting materials. Al-10 %Sr & Al-10 %Sb master alloys were used as modifiers. The elements were melted in an induction furnace using an alumina crucible under an argon atmosphere to minimize oxidation and chemical reactions between the alloy and the metallic die.

To reduce the burning loss of Mg, the casting procedure was the following: 1) Al was melted first at a temperature of 750 °C, 2) Si and Zn were added, and the melt was left to homogenize for a few minutes, 3) Then Mg was added and 5) Finally, once all the elements were melted, Al-10 %Sr & Al-10 %Sb master alloys were added to the modified alloys and the melt was allowed to homogenize for few minutes. Finally, the molten alloy was poured into a stepped structure AISI H13 steel die preheated to 300 °C. The metallurgical analysis primarily concentrated on the initial step of the die, which represents the most significant dimensions, and also due to its practicality in fabricating compression specimens.

For composition analysis, chips machined from the as-cast samples were digested in concentrated nitric acid (HNO_3) and analyzed by inductively coupled plasma optical emission spectrometry (ICP-OES; Thermo Fisher Scientific iCAP 6500 Duo, USA). All measurements were repeated multiple times to ensure repeatability and were listed in Table 1.

After alloy fabrication, solidification and phase-diagram calculations were performed for three alloys— $Al_{60}Zn_{27}Mg_{11}Si_2$ (Alloy 1) and the Sr and Sb modified $Al_{60}Zn_{27}Mg_{11}Si_2 + Sr_{0.021}Sb_{0.001}$ (Alloy 2), and $Al_{60}Zn_{27}Mg_{11}Si_2 + Sr_{0.136}Sb_{0.031}$ (Alloy 3)—using FactSage™ 8.2 software and utilizing the FTlite database [50].

2.2. *Enhancing microstructure via manufacturing methods*

For the second optimization method, the modified alloy $Al_{60}Zn_{27}Mg_{11}Si_2 + Sr_{0.021}Sb_{0.001}$ (Alloy 2)—which exhibited the most favorable properties—was re-melted and re-cast to ensure sufficient dimensions for subsequent processing. The alloy was produced by conventional sand casting (SC) into 300 mm-long cylinders, maintaining the target composition. These cylinders were then subjected to Near-Solidus Forming (NSF) and Directional Solidification (DS). After casting, the chemical composition was re-evaluated to confirm that the nominal alloy chemistry was preserved across all three processing routes, with minor adjustments applied when necessary to compensate for potential elemental losses.

2.2.1. *Near Solidus Forming process*

Near Solidus Forming (NSF) process was performed on the selected alloy using a 400-tonne Fagor AC servomechanical press equipped with NSF tooling developed by Mondragon Unibertsitatea [41]. Fig. 2a shows the NSF cell consisting of an upper and lower die holder linked by four hydraulic cylinders for opening and closing the dies, plus four additional cylinders in the upper holder to prevent die separation.

Dies and forming parameters were designed using Finite-element method simulations in FORGE NxT 3.0. According to FEM simulations, an entry angle of 45° on the conical dies was determined in order to yield a uniform equivalent strain. Fig. 2b shows the dies, made of AISI H13 steel, and forged multicomponent alloy specimens. During each cycle, the punch descends from top dead center to full stroke, reaching the maximum force capacity only at the bottom, where it is held under load for 5 s to compress the material.

The NSF temperature was established by Differential Scanning Calorimetry (DSC), which was conducted on 100 mg samples at a heating rate of 10 °C/min, revealing a solidus of approximately 390 °C. Accordingly, the NSF process was carried out at 95 % of this solidus (≈380 °C).

2.2.2. *Directional solidification process*

For the Directional Solidification (DS) process, the sand-cast cylinder was remelted in an alumina crucible and held at 720 °C under an argon atmosphere with 3 vol% SF_6 as protective gas. The molten alloy was stirred for 20 min to ensure homogeneity and then poured into a boron-nitride-coated steel die to prevent sticking and thermal shock.

Directional solidification was carried out using the setup described by Elsayed et al., [51] which enables controlled cooling through gradual immersion of the die into a water bath. This method generated a steep thermal gradient, promoting rapid directional solidification and

Table 2
Heat treatment of optimized multicomponent light alloys.

Sample	Solution Treatment	
	Step 1	Step 2
Double Homogenization Heat Treatment “DHHT”	325 °C/24 h	380 °C/24 h + Quenching

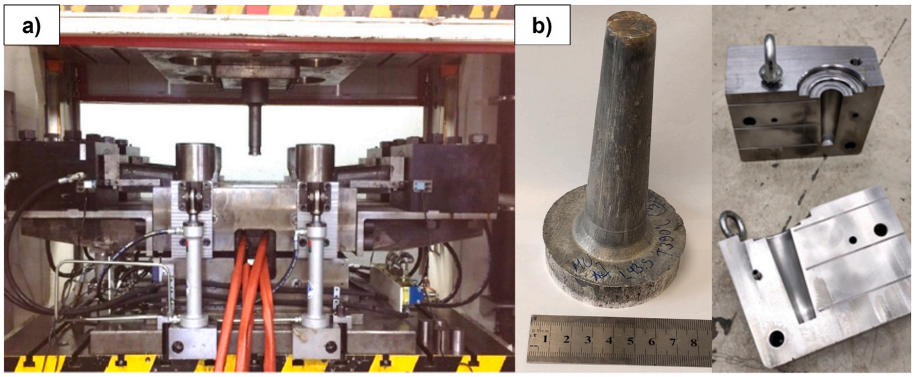

Fig. 2. (a) NSF cell (b) The dies used for the NSF process are made of AISI H13 steel, while the forming specimens are fabricated from the multicomponent alloy.

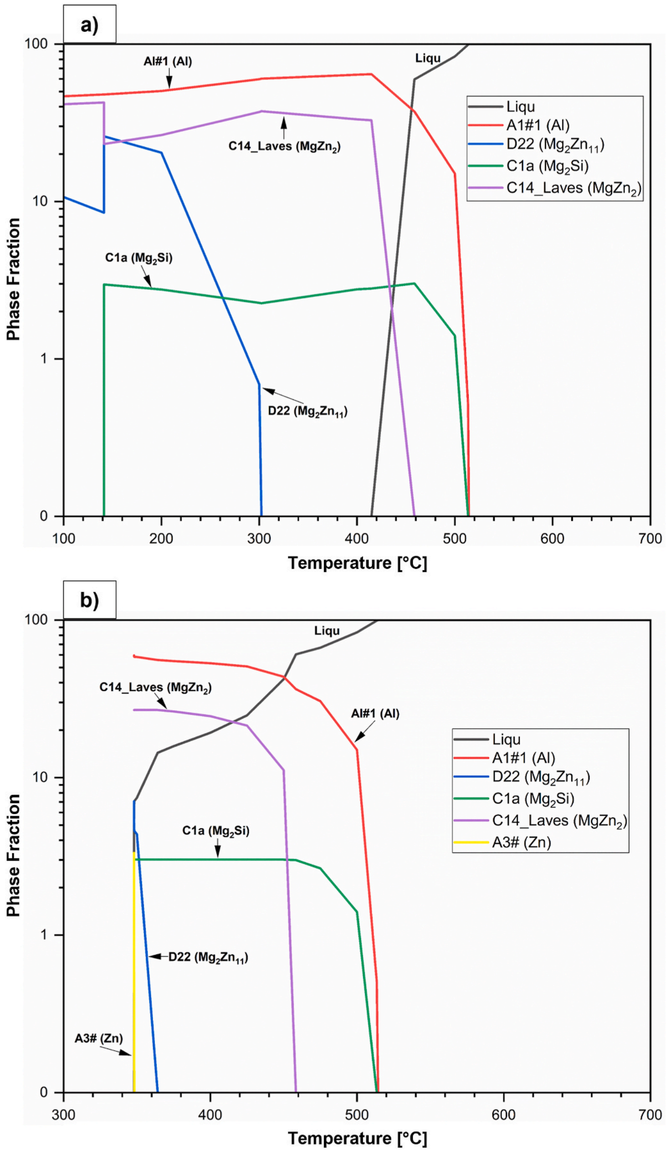

Fig. 3. Solidification simulations for the optimized $Al_{60}Zn_{27}Mg_{11}Si_2$ (Alloy 1), lightweight multicomponent alloy calculated by FactSage (CALPHAD): a) Equilibrium solidification, and b) non-equilibrium solidification (Gulliver -Scheil).

resulting in a refined microstructure with minimal defects. The final cast cylinders measured 180 mm in length and 65 mm in diameter.

2.3. Heat treatments

All samples were subjected to a double-homogenization heat treatment (DHHT) in argon consisting of a two-step solution treatment (Table 2): 325 °C for 24 h (Step 1) followed by 380 °C for 24 h and water quenching (Step 2). The treatment temperatures were selected according to CALPHAD simulations reported in Ref. [20].

2.4. Material characterization

Standard metallographic techniques were applied to study the microstructural features of the samples. Scanning electron microscopy (SEM) and energy-dispersive X-ray spectroscopy (EDS) were performed using an FEI Nova Nano SEM 450 to examine the microstructure and to determine the semiquantitative local chemical composition. Density was measured using the Archimedes method.

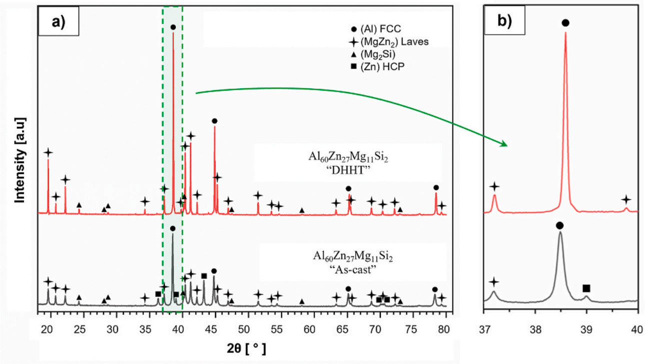

Fig. 4. XRD diffraction patterns for the $Al_{60}Zn_{27}Mg_{11}Si_2$ lightweight multicomponent alloy: a) before and after heat treatment “As-cast” and “DHHT” (Double Homogenization Heat Treatment); comparison of the FCC peak of as-cast and solutionized sample.

Phase analysis was carried out using a Bruker D8 Advance X-ray diffractometer with Cu Kα radiation (λ = 1.5406 Å), operated at 35 kV and 45 mA. Diffraction patterns were collected over 20–100° (2θ) at a scan rate of 4°/min. Patterns were indexed using the PDF-4+ (2021) database from the International Centre for Diffraction Data (ICDD).

Electron Backscatter Diffraction (EBSD) was conducted on selected metallographic samples for phase analysis, using the same FEI Nova Nano SEM 450 operated at 20 kV. A NordlysMax3 detector equipped with a six-diode forescatter system was employed, and the EBSD data were analyzed with AZtecHKL CHANNEL 5 software.

Prior to EBSD, specimens were prepared by standard metallographic methods, followed by final polishing with 0.05 μm colloidal silica for 240 min on a BUEHLER VIBROMET 2 vibratory polisher. This extended polishing step was used to minimize surface damage and ensure the acquisition of high-quality EBSD patterns.

2.5. Mechanical test

Immediately after heat treatments, room temperature compression tests were performed on SC, NSF, and DS samples according to ASTM-E09 standard using a Zwick 050TM universal testing machine. Cylindrical samples of 13 mm diameter and 38 mm length and a strain rate of $0.01s^{-1}$ were used in the compression tests and each test was repeated 3 times.

Hardness (H) and indentation modulus (E) of the alloy’s phases were measured on mirror-polished cross-sections using a NanoTest Vantage4 system at room temperature, following ASTM E2546-07. Surfaces were prepared by grinding and polishing with 1 μm and 0.1 μm α-alumina suspensions.

A Berkovich indenter (three-sided pyramid, 65.3° face angle) applied a maximum load of 10 mN in load-controlled single cycles. Loading and unloading rates were 1 mN/s, with a 20 s hold at peak load. An integrated optical microscope ensured precise indent placement. Hardness and modulus values were extracted from the unloading segment of the load-displacement (P–h) curves. Indentation grids of 10 × 10 imprints (6 μm spacing) were performed in regions containing all phases, yielding 100 measurements per sample.

3. Results

3.1. Optimized composition phases by CALPHAD

CALPHAD simulations on Alloy 1 showed that reducing Si by 2 at.% completely eliminated primary silicon precipitation. Fig. 3a presents the equilibrium solidification sequence for $Al_{60}Zn_{27}Mg_{11}Si_2$: Mg_2Si precipitates first at ≈520 °C, followed by the Al (FCC) phase at ≈510 °C, which reaches its maximum fraction between 310 °C and 410 °C. The

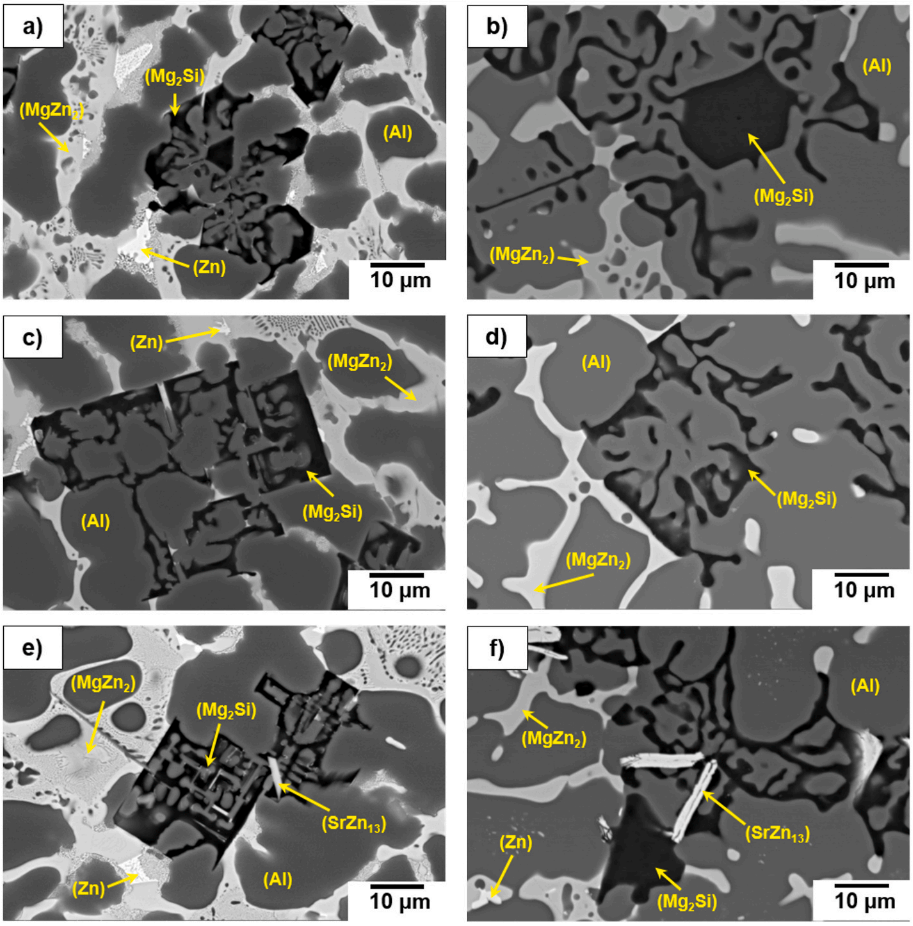

Fig. 5. Backscattered-electron SEM micrographs of Alloy 1 ($Al_{60}Zn_{27}Mg_{11}Si_2$), Alloy 2 ($Al_{60}Zn_{27}Mg_{11}Si_2$ + $Sr_{0\cdot021}Sb_{0\cdot001}$) and Alloy 3 ($Al_{60}Zn_{27}Mg_{11}Si_2$ + $Sr_{0\cdot136}Sb_{0\cdot031}$) showing the as-cast condition in subfigures (a), (c) and (e), respectively, and the heat-treated condition in subfigures (b), (d) and (f), respectively.

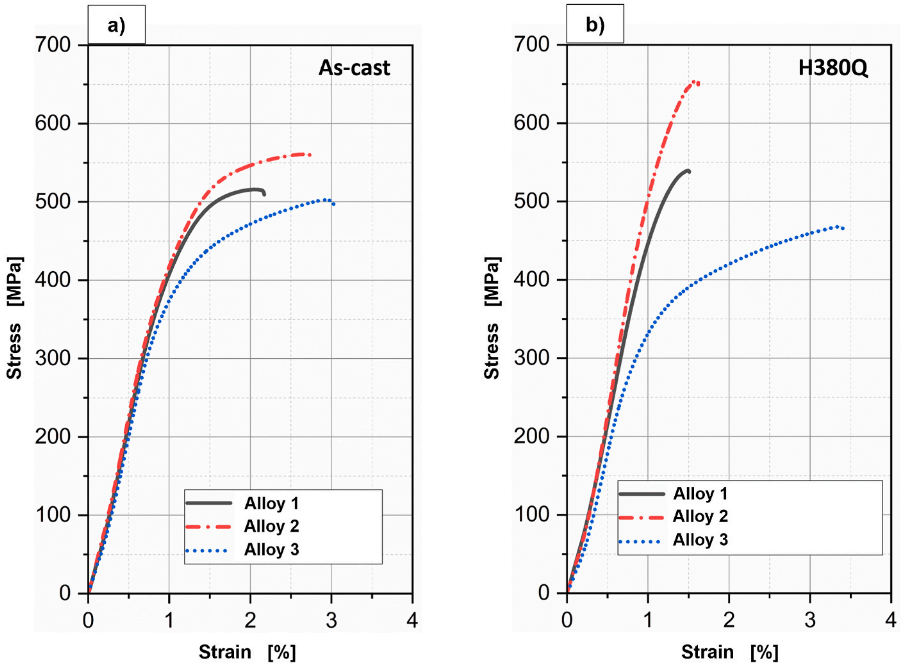

Fig. 6. Uniaxial compression stress–strain curves for Alloy 1 (black), Alloy 2 (red dashed), and Alloy 3 (blue dotted) in the as-cast state (a) and after DHHT (H380Q) heat treatment (b).

Table 3

Compressive mechanical properties of Sr-Sb modified and unmodified $Al_{60}Zn_{27}Mg_{11}Si_2$ alloy at room temperature.

Condition	Alloy	Yield strength (MPa)	Ultimate strength (MPa)
As-cast	Alloy 1	405 ± 5	516 ± 4
	Alloy 2	448 ± 2	560 ± 2
	Alloy 3	345 ± 7	502 ± 11
H380Q	Alloy 1	502 ± 3	539 ± 2
	Alloy 2	560 ± 2	654 ± 2
	Alloy 3	323 ± 15	467 ± 18

Laves phase $MgZn_2$ forms at ≈460 °C, and Mg_2Zn_{11} appears last at ≈320 °C. Under Scheil conditions (Fig. 3b), Mg_2Si, Al (FCC) and $MgZn_2$ again form at the same temperatures, but Mg_2Zn_{11} shifts to ≈360 °C and an HCP Zn phase emerges near 350 °C.

To corroborate the thermodynamic simulations performed by CALPHAD, X-ray diffraction (XRD) was performed on Alloy 1 in both as-cast and heat-treated conditions (Fig. 4). In the as-cast condition, peaks matched Al (FCC, PDF 00-004-0787), $MgZn_2$ (Laves, PDF 04-003-2083), Mg_2Si (PDF 01-083-5235) and Zn (HCP, PDF 01-078-9363), in agreement with the CALPHAD Scheil sequence. In the heat-treated condition (Fig. 4b), Zn peaks are no longer observed, indicating that the HCP Zn phase dissolved into the Al (FCC) matrix.

3.2. Modification of Mg_2Si phase with Sr and Sb addition

In the unmodified Alloy 1 (Fig. 5a), primary Mg_2Si precipitates as blocky particles surrounded by a eutectic network. The addition of Sr and Sb, profoundly alters Mg_2Si morphology in the Al–Zn–Mg–Si system. In alloy 2 (Fig. 5c), primary blocks disappear and only eutectic Mg_2Si forms, evolving into compact square plates with an internal fishbone pattern. For Alloy 3 with higher Sr/Sb levels (Fig. 5e), these plates become even more tightly packed and retain a pronounced fishbone skeleton. In this heavily modified alloy, a new $SrZn_{13}$ intermetallic also appears with a feather-like morphology adjacent to Mg_2Si.

Backscattered-electron SEM images of heat-treated samples (Fig. 5b, d, f) show that the HCP Zn phase dissolves into the Al matrix, leaving only Al(FCC), Laves $MgZn_2$, and Mg_2Si in Alloys 1 and 2 (Fig. 5b and d). In these alloys, Mg_2Si adopts more rounded plate shapes after treatment. In the highly modified alloy (Fig. 5f), the $SrZn_{13}$ phase persists post-treatment—now coarser—and remains closely associated with the compact Mg_2Si plates.

3.3. Compression resistance of chemically optimized alloys

Fig. 6 presents uniaxial compression curves for Alloy 1, Alloy 2 and Alloy 3 in both the as-cast (Fig. 6a) and heat-treated (homogenized and quenched, Fig. 6b) conditions. Yield strength (YS) and ultimate strength (UTS) values are summarized in Table 3.

As-cast, Alloy 2 exhibits the highest performance, with YS = 448 ± 2 MPa and UTS = 560 ± 2 MPa. Alloy 1 follows (YS = 405 ± 5 MPa, UTS = 516 ± 4 MPa) and Alloy 3 shows the lowest values (YS = 345 ± 7 MPa, UTS = 502 ± 11 MPa). After heat treatment (H380Q), Alloy 2 again leads (YS = 560 ± 2 MPa, UTS = 654 ± 2 MPa), Alloy 1 is intermediate (YS = 502 ± 3 MPa, UTS = 539 ± 2 MPa), and Alloy 3 remains lowest (YS = 323 ± 15 MPa, UTS = 467 ± 18 MPa). The superior

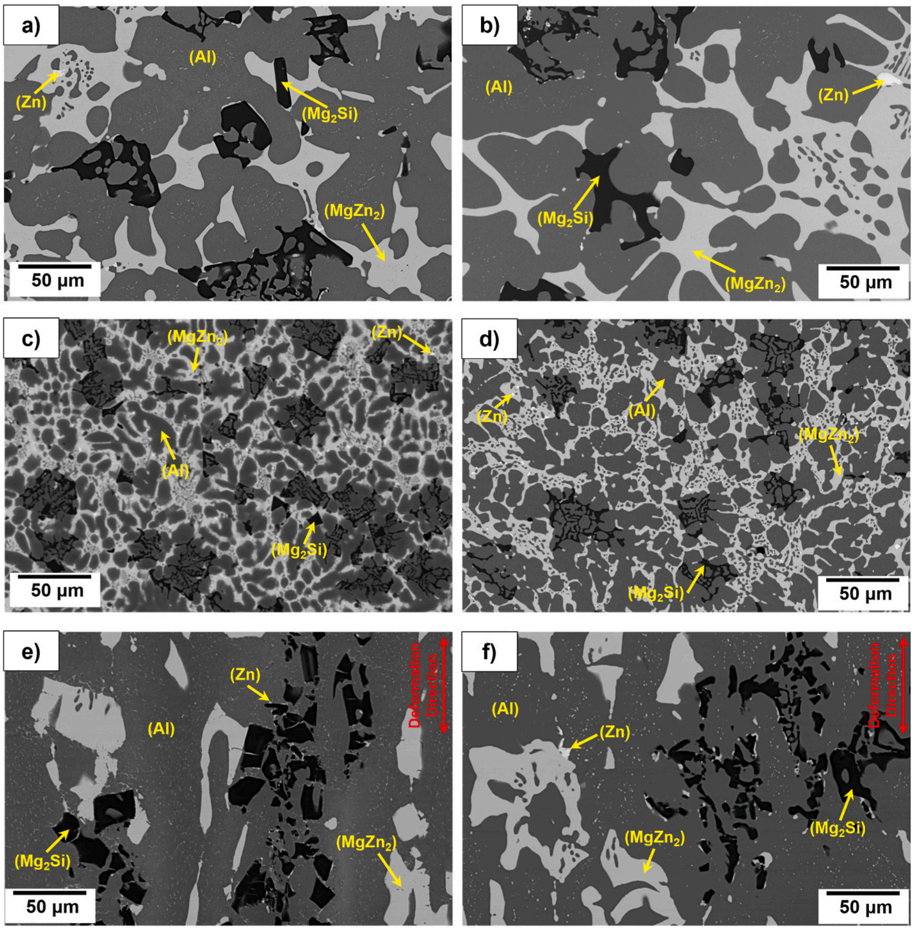

Fig. 7. Backscattered-electron SEM images (50 µm) of the optimized $Al_{60}Zn_{27}Mg_{11}Si_2 + Sr_{0.021}Sb_{0.001}$ alloy processed by SC (a, as-cast; b, after DHHT), DS (c, as-cast; d, after DHHT), and NSF (e, as-formed; f, after DHHT).

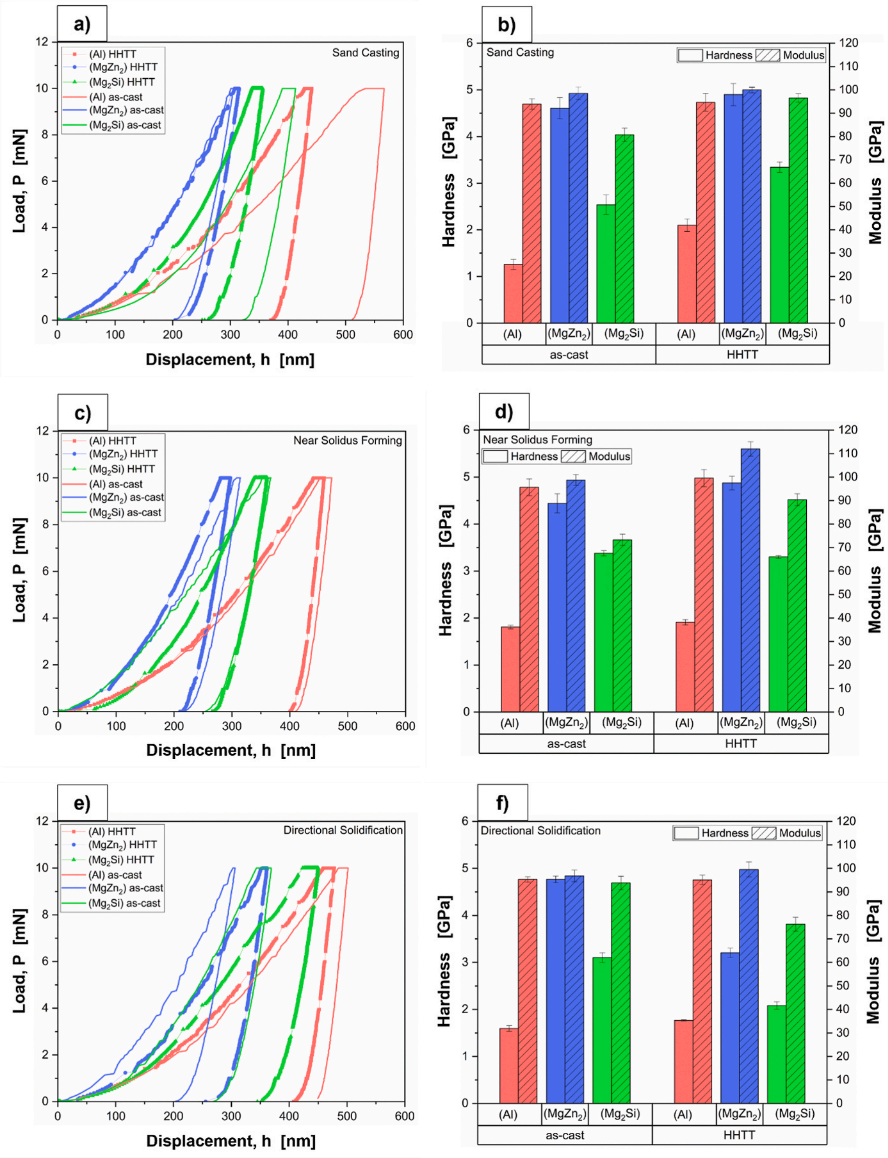

Fig. 8. Nanoindentation results for the chemically optimized Alloy 2 processed by SC, NSF, and DS. Panels show load–displacement curves (a, c, e) and the corresponding hardness and elastic modulus values (b, d, f) for each processing route. (Details of the data used to compute and plot hardness/modulus, as well as the procedure for phase assignment, are provided in the Supplementary Material).

behavior of Alloy 2 reflects its optimized Sr/Sb additions, whereas the higher modifier levels in Alloy 3 lead to reduced strength.

3.4. Microstructural analysis of Alloy 2 through various manufacturing processes

After evidencing the superior properties of Alloy 2, the following micrographs show the microstructure after processing by three different routes—SC, NSF, and DS —each examined both in the as-cast/as-formed and following DHHT. In the as-cast sand casting sample (Fig. 7a), backscattered-electron imaging reveals three distinct regions: dendritic FCC-Al crystals appear as light gray, interdendritic Laves ($MgZn_2$) regions are darker gray, and the eutectic Al + Mg_2Si mixture shows as a mix of medium-gray Al and nearly black Mg_2Si. Bright spots correspond to Zn-rich phases. After DHHT (Fig. 7b), the FCC-Al matrix is noticeably cleaner, with far fewer and more rounded precipitates. Both Laves ($MgZn_2$) and Mg_2Si phases coalesce into small clusters and adopt smoother, more spheroidal morphologies.

Directional solidification in the as-cast state (Fig. 7c) produces a very fine, uniform distribution of phases, although minor segregation bands are still visible. Following DHHT (Fig. 7d), those segregation bands disappear entirely, yielding an even more homogeneous microstructure. The Near Solidus Forming process in the as-formed sample (Fig. 7e) fractures the Laves and Mg_2Si particles and distributes them throughout the matrix. The microstructure shows clear elongation and tear-like features along the direction of applied load.

Upon DHHT of the NSF specimens (Fig. 7f), the fractured Laves and Mg_2Si particles round off, and all signs of plastic deformation vanish. The result is a smooth, defect-free surface with uniformly dispersed precipitates. Processing also strongly affects dendritic morphology. In the DS samples (Fig. 7c–d), a fine, well-defined dendritic network is visible, whereas in the NSF-processed specimens (Fig. 7e and f) the dendritic pattern is largely obscured or broken up by deformation. This contrast highlights how each fabrication route imposes a distinct solidification pathway.

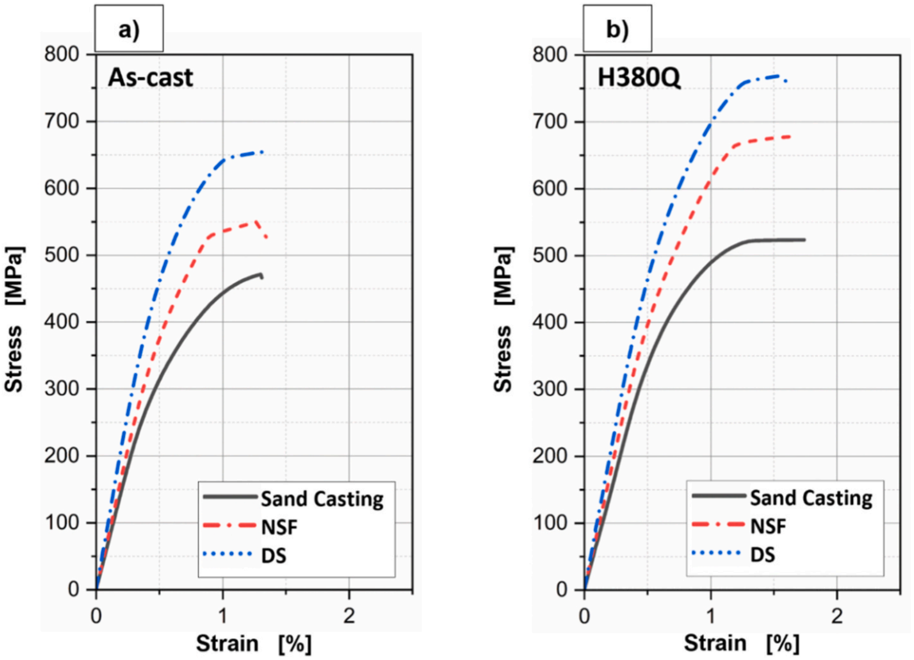

Fig. 9. Uniaxial compression stress–strain curves of the chemically optimized Alloy 2 lightweight multicomponent alloy processed by sand casting (black solid line), near-solidus forming (red dashed line), and directional solidification (blue dash-dot line): (a) as-cast condition; (b) after double-homogenization heat treatment DHHT (H380Q).

3.5. Phase hardness and elastic modulus after DC, NSF, and DS

Nanoindentation of a lightweight multicomponent alloy processed by sand casting, near-solidus forming, and directional solidification (Fig. 8a,c,e) showed via load-depth curves that Al-FCC matrix, Mg_2Si, and $MgZn_2$ (Laves) phases become harder and stiffer after heat treatment—especially in sand-cast and near-solidus samples—while $MgZn_2$ remains the hardest and stiffest phase under all conditions.

In SC material (Fig. 8a and b) Al-FCC penetration depth decreases from 566 nm to 441 nm (hardness 1.26 → 2.09 GPa, modulus 94 → 95 GPa), Mg_2Si from ≈413 nm to 356 nm (2.54 → 3.34 GPa, 81 → 96 GPa) and $MgZn_2$ stays at ≈305 nm (4.60 → 4.89 GPa, 99 → 100 GPa).

NSF (Fig. 8c and d) yields Al-FCC ≈472 → 460 nm (1.80 → 1.91 GPa, 95 → 99 GPa), Mg_2Si ~ 366 nm unchanged (3.38 → 3.30 GPa, 73 → 90 GPa) and $MgZn_2$ 366 → 297 nm (4.44 → 4.87 GPa, 99 → 112 GPa).

In DS (Fig. 8e and f) Al-FCC goes from 501 to 477 nm (1.59 → 1.76 GPa, 95 GPa), Mg_2Si measures 369 nm after treatment (3.10 → 2.08 GPa, 94 → 76 GPa) and $MgZn_2$ 369 → 362 nm (4.76 → 3.20 GPa, 97 → 99 GPa)—here, unlike other routes, heat treatment actually softens both intermetallics.

Consequently, while all processing routes can be tuned via heat treatment to enhance overall hardness and stiffness, NSF with subsequent tempering offers the most balanced reinforcement across phases. In contrast, post-treatment softening in DS may limit composite strength but can increase ductility and improve crack-propagation resistance through the controlled softening of these intermetallic phases.

3.6. Compression resistance after SC, NSF, and DS

The true stress–strain curves in Fig. 9a show that, in the as-processed condition, the DS alloy achieves the highest compressive strength (658 MPa), followed by the NSF alloy (552 MPa) and the sand-cast alloy (471 MPa). After double homogenization and solution treatment (Fig. 9b), all three alloys exhibit substantial strength gains: DS rises to 769 MPa, NSF to 679 MPa, and sand-cast to 647 MPa. Compared to their as-processed states, the strength of the sand-cast alloy increased by ~38 % after heat treatment, that of the NSF alloy by ~23 %, and that of the DS alloy by ~17 %. This indicates that the most significant relative hardening occurs in the sand-cast microstructure, whereas DS retains the highest absolute strength both before and after heat treatment.

3.7. Fractographic observations

Figs. 10–12 compare compression crack-path micrographs of optimized Alloy 2 processed by SC, NSF, and DS, both as-cast and heat-treated. In every case, cracks nucleate and grow through interdendritic regions, cutting primarily through brittle Laves ($MgZn_2$) phase and occasionally linking to Mg_2Si particles, while Al-FCC matrix remains uncracked and arrests further propagation. Fractography shows a classic cleavage morphology—with bright, reflective facets and no signs of plastic deformation—consistent with lack of active slip systems in hexagonal C14 Laves structure at room temperature. This brittleness, driven by interplanar locking and complex atomic arrangements, explains high strength but low ductility in all three processing routes [52–54].

4. Discussion

4.1. Composition optimization analysis

Primary Si in lightweight alloys degrades mechanical performance because its coarse, brittle nature (near-zero elongation) promotes crack initiation and provides easy pathways for crack propagation. Even small primary Si particles are linked by flaky eutectic Si, which further channels cracks and limits ductility gains [55–57]. To counteract this, researchers have developed modification treatments that refine primary Si, thereby enhancing alloy ductility [58–60]. CALPHAD modeling of $Al_{58}Zn_{28}Mg_6Si_8$ revealed that reducing Si content—while preserving a high solid-solution matrix—suppresses primary Si precipitation. The resulting optimized composition, $Al_{60}Zn_{27}Mg_{11}Si_2$, was validated by SEM (Fig. 5a–b) and XRD (Fig. 4), which identified only four phases: FCC Al, C14 Laves ($MgZn_2$), Mg_2Si, and HCP Zn. Notably, the CALPHAD-predicted Mg_2Zn_{11} phase was absent in both SEM and XRD analyses.

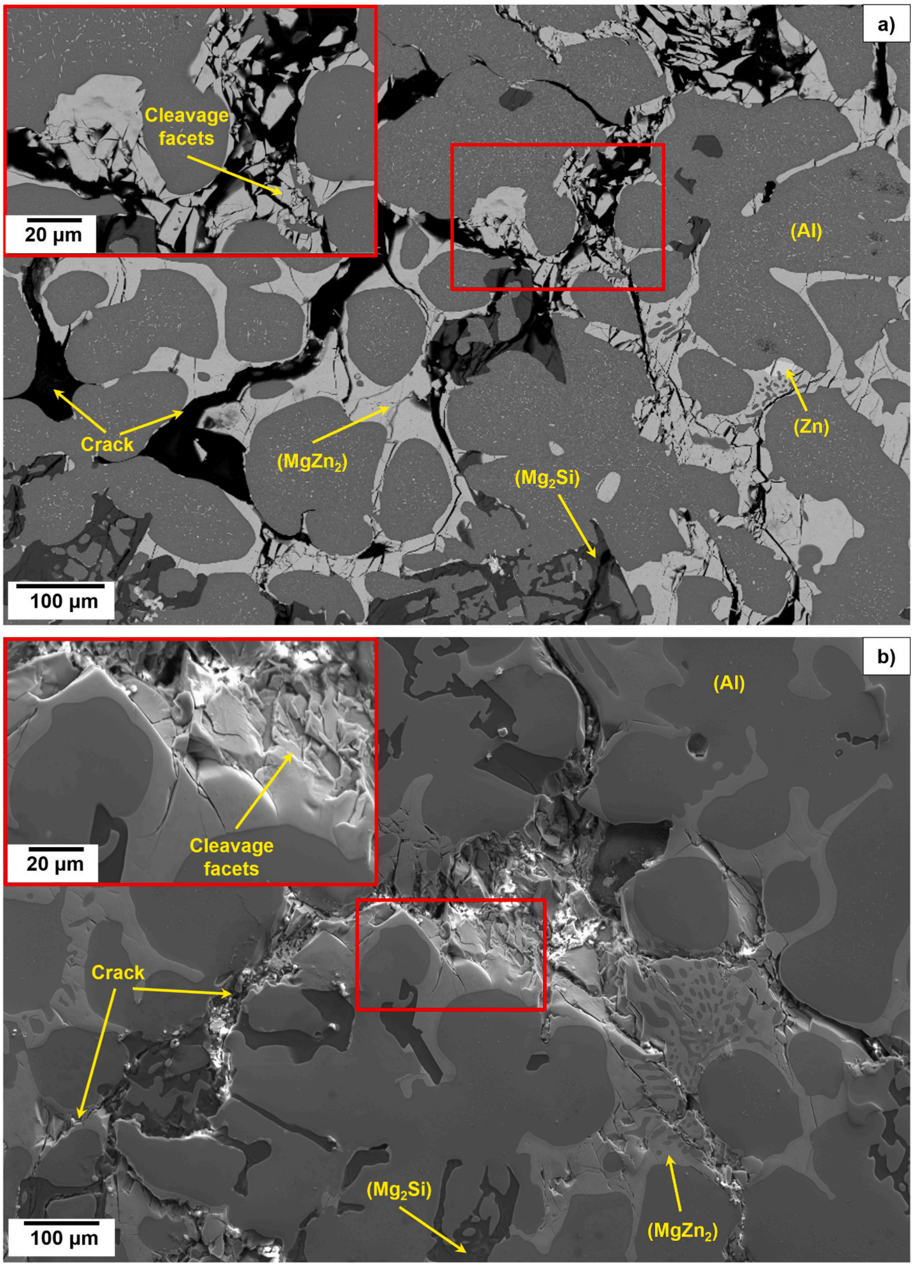

Fig. 10. Crack-Path Micrograph in a Compression Specimen of the multicomponent alloy $Al_{60}Zn_{27}Mg_{11}Si_2$ under the following conditions: a) SC "As-cast", and b) SC "Heat-treated" (Cleavage crack initiated in Laves phase $MgZn_2$).

4.2. Mechanisms for the modification and refinement of the Mg_2Si phase

Chen et al. [27] identified two primary strategies for refining Mg_2Si grains in Al-based alloys. First, enhancing heterogeneous nucleation by introducing potent nucleants into the melt, thereby increasing the number of Mg_2Si nuclei and reducing grain size. Second, grain growth is suppressed through controlled solidification conditions, which limit post-nucleation coarsening rather than increasing the nucleation rate.

Yang et al. [60] demonstrated these principles in AZ61-0.7Si alloys: 0.4 wt % Sb addition refined Mg_2Si without changing its morphology, while 0.12 wt % Sr transformed Mg_2Si from coarse, script-like particles into fine, irregular grains. Thus, effective heterogeneous nucleation requires a crystallographic misfit below ~6 % between the nucleant and Mg_2Si planes [22]. These effects correlate with atomic-plane mismatches of 1.72 % for (0001)Mg_3Sb_2//(111)Mg_2Si and 0.69 % for (100) Al_4Sr//(100)Mg_2Si—both below the 6 % threshold—confirming Mg_3Sb_2 and Al_4Sr as effective heterogeneous nuclei.

CALPHAD isopleths for $Al_{60}Zn_{27}Mg_{11}Si_2Sb_{0.13}Sr_x$ (Fig. 13) predict Mg_3Sb_2 as the primary precipitate; at higher Sr/Sb levels (Alloy 3), $SrSi_2Al_2$ forms (stable 460–560 °C), and Sr dissolves into Mg_2Si, suggesting partial Si substitution. Moreover, Dong et al. [61] found that Sr addition to AZ61 shifts eutectic Mg_2Si morphology from Chinese-script to polygonal, with dissolved Sr atoms altering growth kinetics and improving particle morphology. Al_4Sr that solidifies concurrently serves as additional nucleation sites, further refining Mg_2Si. Similar mechanisms likely apply in Alloys 2 and 3.

Finally, the $SrZn_{13}$ phase—predicted by CALPHAD (Fig. 13) is confirmed by EBSD in Alloy 3 (Fig. 14) and exhibits a feather-like morphology embedded in Mg_2Si. Bilbao et al. [62] observed $SrZn_{13}$ formation in $Al_{58}Zn_{28}Mg_6Si_8$ between 30 °C and 280 °C via X-ray thermo-diffraction, noting Sr–Zn interaction. Small Sr additions (~0.1 wt %) in Zn-Al alloys enhance strength and ductility by forming $SrZn_{13}$

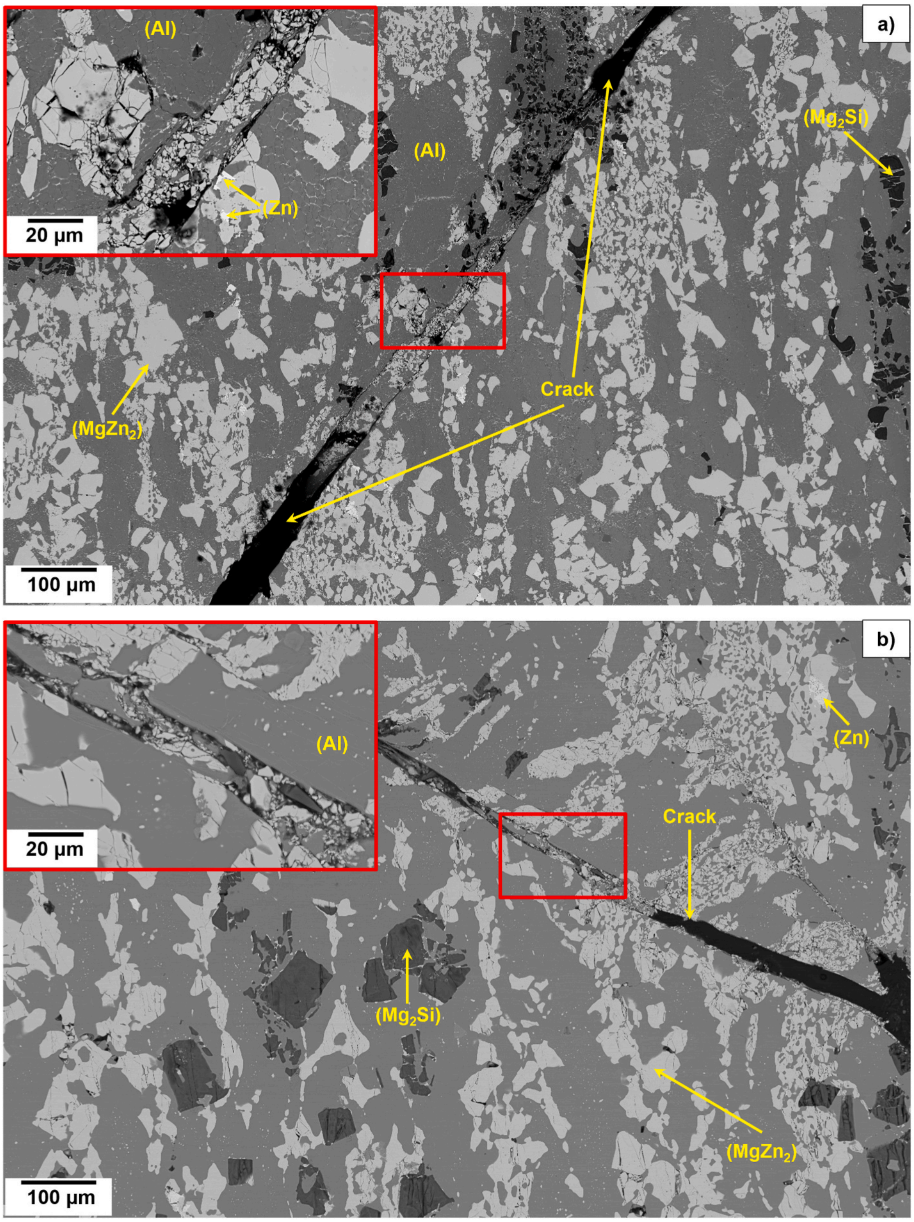

Fig. 11. Crack-Path Micrograph in a Compression Specimen of the multicomponent alloy $Al_{60}Zn_{27}Mg_{11}Si_2$ under the following conditions: a) NSF “As-cast”, and b) NSF “Heat-treated”.

nucleation sites [63,64], but excessive Sr (≥0.8 wt %) coarsens $SrZn_{13}$ and reduces strength. In Alloy 3, higher Sr/Sb levels produce larger $SrZn_{13}$ particles that significantly degrade tensile strength.

4.3. *Effect of different processing techniques on the $Al_{60}Zn_{27}Mg_{11}Si_2$ alloy*

The influence of different manufacturing routes—DC, NSF, and DS—on the microstructure and compressive mechanical properties of the Sr- and Sb-modified $Al_{60}Zn_{27}Mg_{11}Si_2$ alloy was systematically investigated. Different manufacturing processes lead to variations in phase size, phase distribution, and alloy morphology, as observed through microstructure analysis. The DS process, for instance, produces a fine microstructure with a homogeneous distribution of phases. The higher cooling rate during solidification results in the formation of a finer lamellar-dendritic structure. The lamellar interface is considered an effective barrier to the motion of dislocations, leading to the accumulation of dislocations on slip planes at the lamellar interface [65,66]. Due to the reduced mean free path of dislocations in the material, the directional solidification $Al_{60}Zn_{27}Mg_{11}Si_2$ alloy with a refined lamellar structure exhibits the highest yield strength of 650 MPa.

In the NSF process, the microstructure of the samples is finer compared to sand casting, resulting in a unique structure. This is achieved through specific process conditions, such as high shear during alloy flow, rapid cooling, pressure applied during solidification, and the consequent formation of a strong non-equilibrium state of the material [39,40,67]. The careful selection of parameters ensures that the NSF die is defect-free, with complete filling of the metal in the die cavity and absence of microporosity. The observed increase in yield strength of 540 MPa in the alloys processed by NSF, compared to sand-cast alloys with a yield strength of 450 MPa, can be attributed to the fracture and dispersion of (Mg_2Si) phases, particularly the Laves phase ($MgZn_2$), during the NSF process. By disrupting the continuity of the Laves phase, crack propagation is hindered, and it gets arrested within the FCC aluminum matrix or the (Mg_2Si) intermetallic phase until it encounters a critical resolved shear stress (CRSS) value. This CRSS is necessary to

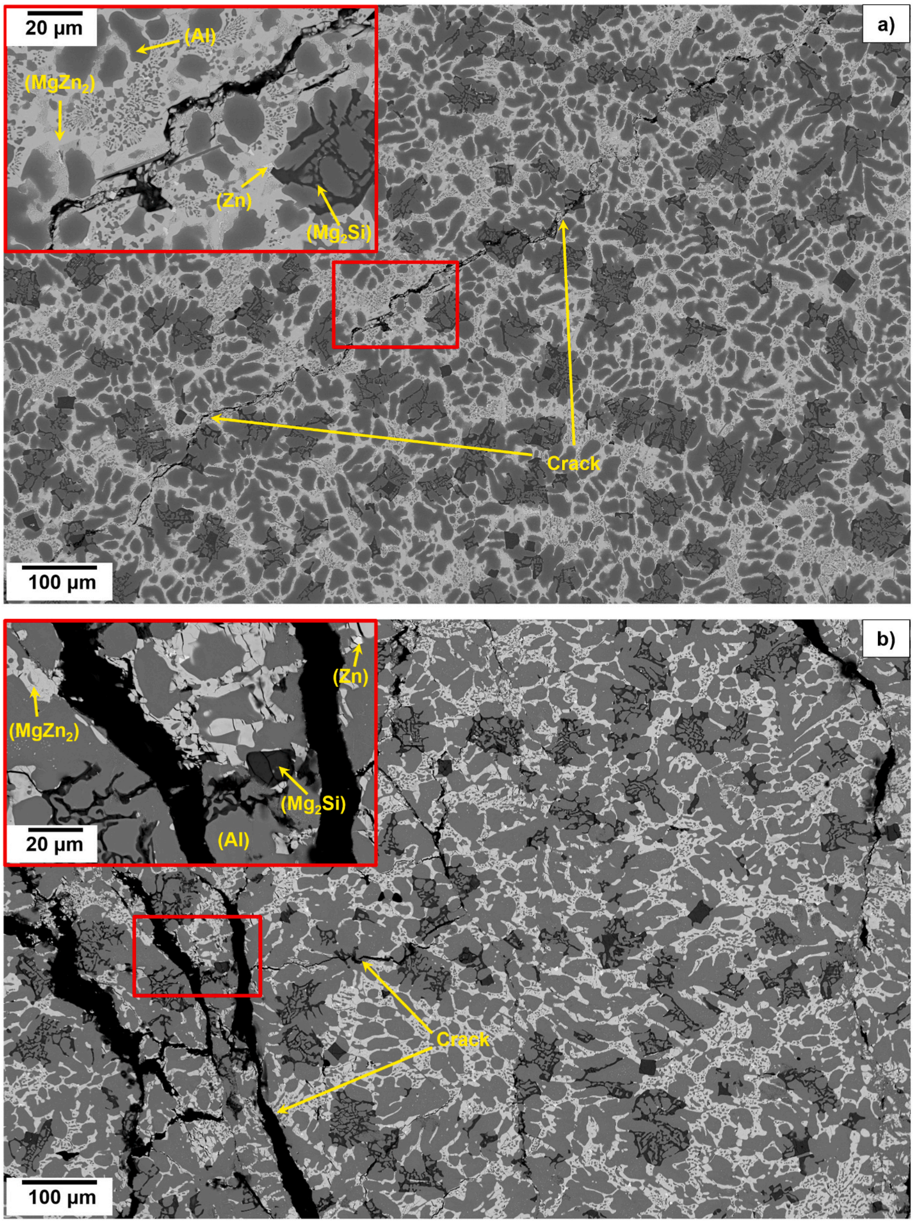

Fig. 12. Crack-Path Micrograph in a Compression Specimen of the multicomponent alloy $Al_{60}Zn_{27}Mg_{11}Si_2$ under the following conditions: a) DS “As-cast”, and b) DS “Heat-treated”.

overcome the resistance to dislocation motion and initiate plastic deformation. These results underscore the critical role of processing route selection in tailoring the microstructural architecture and mechanical response of multicomponent alloys for specific performance requirements.

Regardless of the manufacturing route (sand casting, NSF, or DS) and whether heat treatment is applied, cracks preferentially initiate and/or propagate in the Laves phase ($MgZn_2$). As shown in Fig. 15, fractured $MgZn_2$ particles are frequently observed along crack paths, indicating that this brittle intermetallic acts as a favored locus for damage.

4.4. Correlation between phase-level hardness and compression strength

The correlation between compressive strength (Fig. 9) and nanoindentation response (Fig. 8) arises from the phase-specific mechanical behavior under heat treatment across the different processing routes. Sand casting exhibits the most pronounced relative strength enhancement (~38 %) upon heat treatment, increasing from 471 to 647 MPa. This behavior is consistent with substantial phase hardening, as evidenced by increased hardness values for Al-FCC (+0.83 GPa), Mg_2Si (+0.80 GPa), and $MgZn_2$ (+0.29 GPa), along with a marked reduction in indentation depth. Near-solidus forming (NSF) yields intermediate results, showing moderate gains in both phase hardness (particularly Al-FCC and $MgZn_2$) and compressive strength (~23 % increase, reaching 679 MPa).

Directional solidification results in the highest ultimate compressive strengths, reaching 658 MPa in the as-processed state and 769 MPa after DHHT (H380Q). This superior mechanical performance corresponds to a combination of relatively deep penetration in the Al-FCC phase (~501 nm) and shallow indentation in $MgZn_2$ (~369 nm), reflecting a microstructure enriched in stiff and hard phases. Furthermore, the fine lamellar-dendritic microstructure produced by DS significantly reduces the average phase size, which promotes dislocation pile-up at phase boundaries.

According to the Hall–Petch relationship, the reduction in characteristic microstructural dimensions (e.g., grain or phase size) increases

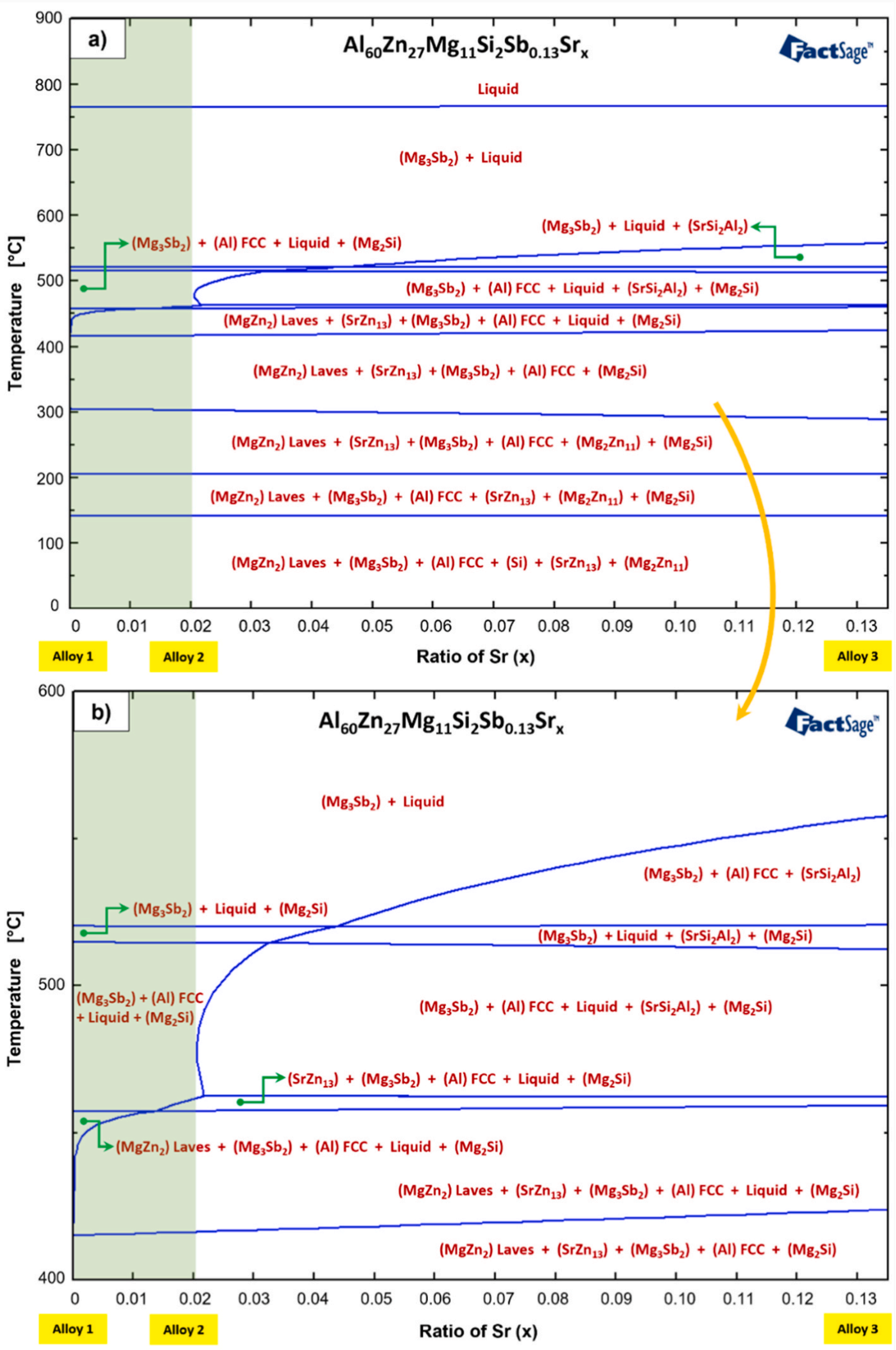

Fig. 13. Phase diagram prediction. a) Isopleth of $Al_{60}Zn_{27}Mg_{11}Si_2Sb_{0.13}Sr_x$ highlighting the composition ranges for each alloy, from the unmodified alloy (Alloy 1) to those modified with Sr and Sb (Alloy 2 and Alloy 3) b) Zoom of isopleth diagram.

the yield strength due to the enhanced barrier effect against dislocation motion. This grain/phase refinement mechanism further contributes to the observed strength enhancement in DS-processed alloys. The macroscopic load-bearing capacity of the alloy is thus governed by the volume fraction and distribution of hard, crack-resistant intermetallic and Laves phases, as well as their respective responses to homogenization and solution treatment.

4.5. *Effect of the heat treatment on $Al_{60}Zn_{27}Mg_{11}Si_2$ alloy*

Fig. 7 illustrates the microstructure of the Sr- and Sb-modified $Al_{60}Zn_{27}Mg_{11}Si_2$ alloy processed using the three different methods: SC, NSF, and DS. The microstructures are shown both before and after undergoing solution treatment. It is evident that segregation has been eliminated in all the microstructures, and the intermetallic phases (Mg_2Si) and $(MgZn_2)$ have become rounded, regardless of the processing method, following solubilization treatment.

The XRD patterns in Fig. 4a revealed that the (Zn) phase, which was detected as a precipitate in the as-cast sample, was completely dissolved into the FCC matrix after solution treatment. Consequently, the FCC lattice size increased due to the dissolution of Mg, Si, and Zn into the matrix. Additionally, the coherence between the sizes of adjacent FCC lattices improved throughout the structure. This conclusion was inferred from the XRD results shown in Fig. 4b, where the two FCC peaks merged

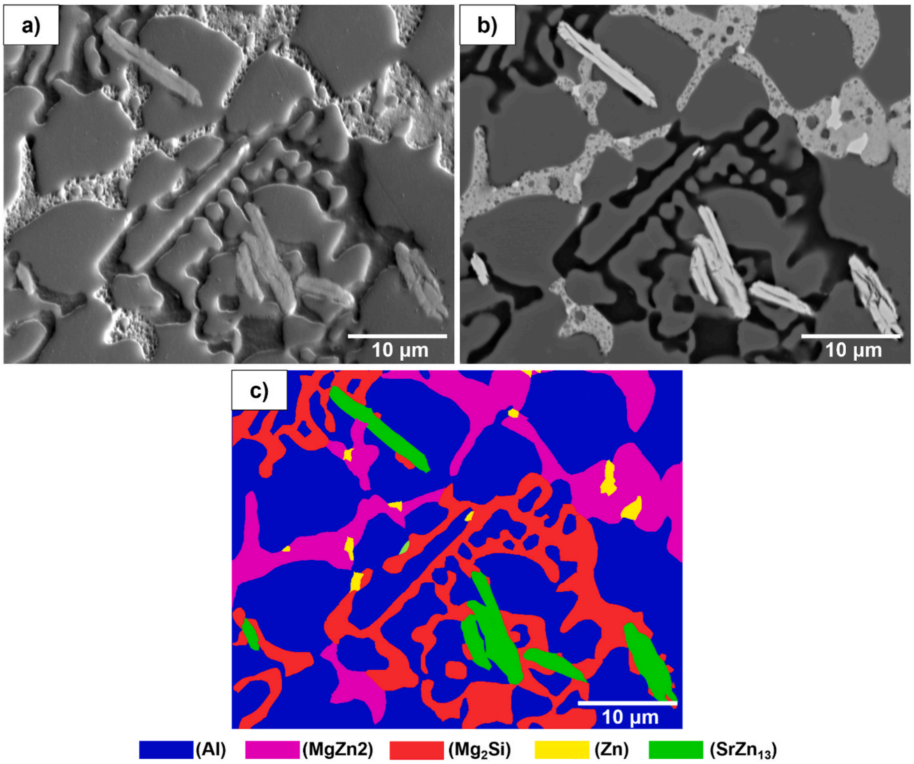

Fig. 14. Phase mapping of the $Al_{60}Zn_{27}Mg_{11}Si_2 + Sr_{0.136}Sb_{0.031}$ (Alloy 3): a) SEM Secondary electron (SE) image, b) Backscattered electron (BSE) image, and c) Hough transform EBSD map with user-selected libraries for (Al), ($MgZn_2$), (Mg_2Si), (Zn) and ($SrZn_{13}$).

into a broadened peak after solution treatment, indicating an increase in FCC lattice size coherency. This increase in FCC lattice size coherency, or coherency strain, is believed to minimize lattice misfit and enhance mechanical properties [68,69].

After undergoing heat treatment, the SC alloy exhibited a significant increase in ultimate compressive strength, reaching 523 MPa, while the DS alloy displayed an increase to 769 MPa. Similarly, the NSF alloy achieved a compressive strength of 679 MPa. This remarkable enhancement in strength was accomplished through the process of solution treatment, involving the dissolution and dispersion of an alloying element into the (Al) FCC matrix. This resulted in the generation of a solid solution-strengthening mechanism [34,68,70].

In the sand-cast alloy, the as-cast condition shows small precipitates in the (Al) FCC matrix—Zn-rich particles, as shown in Fig. 16 and previously identified by Trujillo et al. [20]. After solutionizing and quenching, the strength increases by ~38 % (471 → 647 MPa) and the matrix hardness rises from ~1.26 to ~2.09 GPa (indent depth 566 → 441 nm). This response indicates that solid-solution strengthening is the dominant mechanism: dissolution/redistribution of Mg, Zn, and Si removes segregation, smooths and rounds intermetallic interfaces, and produces solute supersaturation, which elevates the critical stress for slip via solute–dislocation friction (Fleischer/Labusch) [71–73]. The resulting microstructural homogeneity also reduces crack-initiation sites.

5. Conclusions

In this study, we optimized the multicomponent lightweight alloy $Al_{58}Zn_{28}Mg_6Si_8$ to $Al_{60}Zn_{27}Mg_{11}Si_2$, confirming by CALPHAD/SEM the suppression of primary Si while retaining a high Al-fcc solid-solution fraction. Co-modification with Sr/Sb converts Mg_2Si to exclusively eutectic with compact/squared (“fishbone”) morphologies via heterogeneous nucleation at Mg_3Sb_2 and Al_4Sr. There is an optimum modifier window: an intermediate Sr/Sb level maximizes strength, whereas excessive additions promote coarse $SrZn_{13}$ and reduce strength. Despite strength/hardness gains, ductility remains very low, indicating that modifying Mg_2Si alone is insufficient. Processing strongly governs performance. Directional solidification (DS) yields the highest compressive strengths—658 MPa (as-cast) and 769 MPa (post-HT)—through a fine lamellar-dendritic microstructure. Near-Solidus Forming (NSF) also improves strength over sand casting by ~ 17 % (as-cast) and ≈5 % (post-HT). Nanoindentation explains these trends: a robust phase-hardness hierarchy ($MgZn_2 > Mg_2Si >$ Al-FCC) plus phase refinement/distribution—especially under DS—controls macroscopic strength; in SC/NSF, heat treatment hardens phases and raises strength, while in DS the fine architecture dominates even if intermetallics soften slightly. The $MgZn_2$ (Laves) phase acts as a crack initiator; its suppression or morphological control is essential to enhance toughness.

As a benchmark, Fig. 17 compares compressive yield strength versus density for multicomponent lightweight alloys. The blue point ($Al_{58}Zn_{28}Mg_6Si_8$) is the base alloy; the red point corresponds to the best-performing condition developed here—Directional Solidification plus heat treatment. This optimization increases σ_Y from 0.41 to 0.55 GPa (+34 %) while density rises from 3.46 to 3.60 g cm^{-3} (+4 %), yielding an ~28 % gain in specific strength. On the map, the shift is predominantly vertical (↑ strength) with minimal mass penalty, keeping the alloy within the low-density regime. In the literature, many multicomponent lightweight alloys attain high strengths but suffer from limited ductility due to brittle precipitates; others trade higher ductility for increased density. Against that backdrop, the optimized alloy in Fig. 17 improves its relative position (↑ strength with only a modest increase in ρ). Although ductility remains constrained, the combination of high hardness and low density makes it attractive for wear-resistant applications.

6. Future work

Explore a hybrid route that combines directional solidification (DS) with near-solidus forming (NSF) to achieve further microstructural

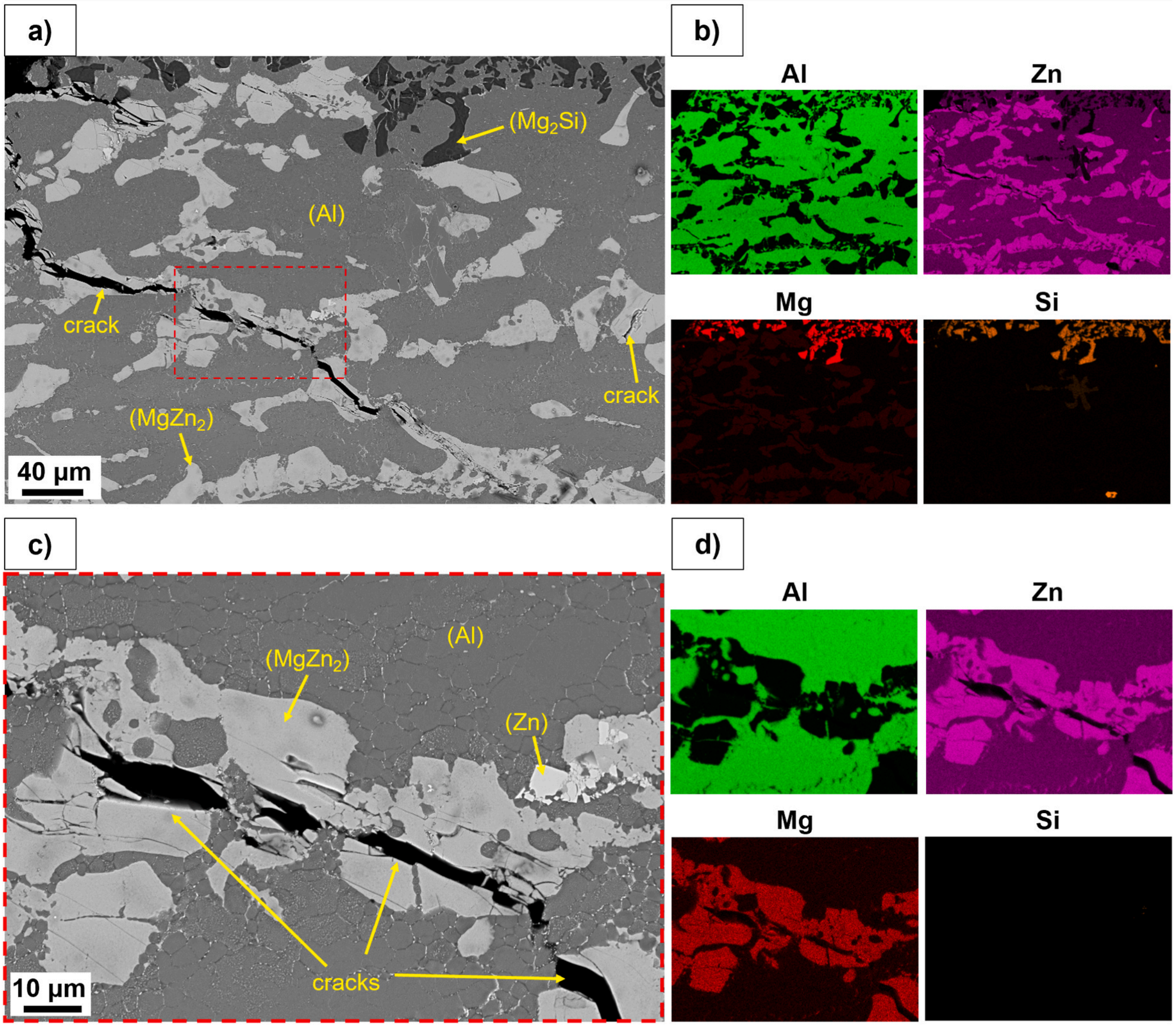

Fig. 15. Fractured regions of the NSF alloys in the as-cast condition. (a, c) Backscattered-electron (BSE) micrographs; (c) is a magnified view of the dashed region in (a). (b, d) Energy-Dispersive X-ray Spectroscopy (EDS) elemental maps (Al, Mg, Zn, Si) corresponding to the fields of view in (a) and (c), respectively. The Laves phase ($MgZn_2$) is frequently observed along crack paths, suggesting a role in crack initiation and/or propagation.

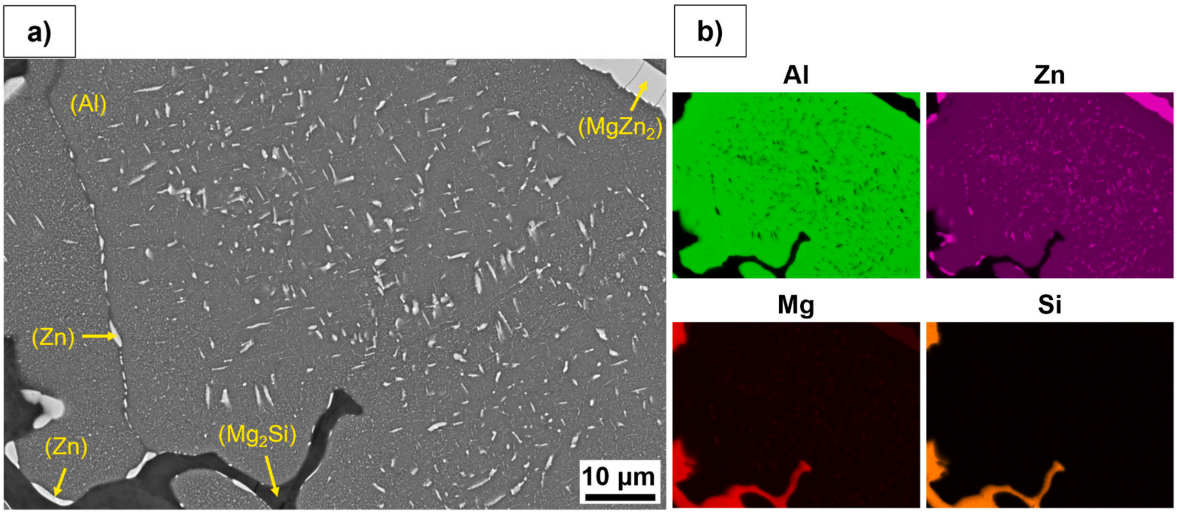

Fig. 16. Micrograph of the sand-cast alloy in the as-cast condition. (a) BSE micrograph; (b) EDS elemental maps (Al, Mg, Zn, Si). Small precipitates within the (Al) FCC matrix correspond to the Zn phase, as evidenced by the EDS maps and previously reported by Trujillo et al. [20].

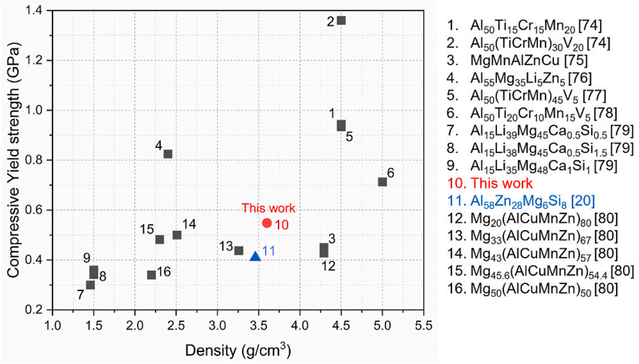

Fig. 17. Compressive yield strength (σ_Y) versus density (ρ) for multicomponent lightweight alloys. The blue marker denotes the base alloy $Al_{58}Zn_{28}Mg_6Si_8$; the red marker shows the optimized condition obtained by directional solidification plus heat treatment [74–80].

refinement and enable simultaneous gains in strength and ductility in lightweight multicomponent alloys. Prioritize ductility by controlling the morphology/continuity of Laves ($MgZn_2$) phases and by optimizing process parameters that promote plasticity.

Declaration of competing interest

The authors declare that they have no known competing financial interests or personal relationships that could have appeared to influence the work reported in this paper.

Acknowledgments

The authors gratefully acknowledge the financial support, encouragement, and guidance provided by the Basque Government through the Elkartek projects KK-2024/00061 and KK-2024/00021. We also wish to express our sincere thanks to the Institute of Materials and Process Design at Helmholtz-Zentrum Hereon for granting access to their casting facilities, and to the Chair of Metal Forming and Casting at the Technical University of Munich for providing access to the nanoindentation facilities.

Appendix A. Supplementary data

Supplementary data to this article can be found online at https://doi.org/10.1016/j.jmrt.2025.11.149.

References

[1] Kashaev N, Ventzke V, Çam G. Prospects of laser beam welding and friction stir welding processes for aluminum airframe structural applications. J Manuf Process 2018;36:571–600. https://doi.org/10.1016/j.jmapro.2018.10.005.

[2] Çam G, Günen A. Challenges and opportunities in the production of magnesium parts by directed energy deposition processes. J Magnesium Alloys 2024;12:1663–86. https://doi.org/10.1016/j.jma.2024.05.004.

[3] Bozkurt Y, Avşar A, Korgancı M, Çam G. A comprehensive review on friction stir additive manufacturing of various structural alloys for aerospace applications. Progress in Additive Manufacturing 2025;10:7365–90. https://doi.org/10.1007/s40964-025-01160-y.

[4] Çam G, İpekoğlu G. Recent developments in joining of aluminum alloys. Int J Adv Manuf Technol 2017;91:1851–66. https://doi.org/10.1007/s00170-016-9861-0.

[5] Li Z, Pradeep KG, Deng Y, Raabe D, Tasan CC. Metastable high-entropy dual-phase alloys overcome the strength–ductility trade-off. Nature 2016;534:227–30. https://doi.org/10.1038/nature17981.

[6] Gao MC, Yeh J-W, Liaw PK, Zhang Y, editors. High-entropy alloys. Cham: Springer International Publishing; 2016. https://doi.org/10.1007/978-3-319-27013-5.

[7] Rogal Ł. On the microstructure and mechanical properties of the AlCoCrCuNi high entropy alloy processed in the semi-solid state. Mater Sci Eng, A 2018;709:139–51. https://doi.org/10.1016/j.msea.2017.10.012.

[8] Emamy M, Nemati N, Heidarzadeh A. The influence of Cu rich intermetallic phases on the microstructure, hardness and tensile properties of Al–15% Mg2Si composite. Mater Sci Eng, A 2010;527:2998–3004. https://doi.org/10.1016/j.msea.2010.01.063.

[9] Heidarzadeh A, Emamy M, Rahimzadeh A, Soufi R, Sohrabi Baba Heidary D, Nasibi S. The effect of copper addition on the fluidity and viscosity of an Al-Mg-Si alloy. J Mater Eng Perform 2014;23:469–76. https://doi.org/10.1007/s11665-013-0794-6.

[10] Chiu Y, Chung T, Yen S, Yu C, Lin W, Hsieh C, et al. Alternating Cu segregation and its stabilization mechanism for coherent η' precipitates in Al–Zn–Mg–Cu alloys. Mater Today Adv 2024;23:100517. https://doi.org/10.1016/j.mtadv.2024.100517.

[11] He B, Cao L, Wu X, Tang S, Lin X, Zou Y. Effect of continuous retrogression and re-ageing treatment on mechanical properties, corrosion behavior and microstructure of an Al-Zn-Mg-Cu alloy. J Alloys Compd 2024;970:172592. https://doi.org/10.1016/j.jallcom.2023.172592.

[12] Zhou SY, Su Y, Wang H, Enz J, Ebel T, Yan M. Selective laser melting additive manufacturing of 7xxx series Al-Zn-Mg-Cu alloy: cracking elimination by co-incorporation of Si and TiB2. Addit Manuf 2020;36:101458. https://doi.org/10.1016/j.addma.2020.101458.

[13] Wagner JA, Shenoy RN. The effect of copper, chromium, and zirconium on the microstructure and mechanical properties of Al-Zn-Mg-Cu alloys. Metall Trans A 1991;22:2809–18. https://doi.org/10.1007/BF02851375.

[14] Ryum N. Precipitation and recrystallization in an A1-0.5 WT.% Zr-alloy. Acta Metall 1969;17:269–78. https://doi.org/10.1016/0001-6160(69)90067-4.

[15] Tai C-L, Pua Y-M, Chung T-F, Yang Y-L, Chen H-R, Chen C-Y, et al. The effect of minor addition of Mn in AA7075 Al–Zn–Mg–Cu aluminum alloys on microstructural evolution and mechanical properties in warm forming and paint baking processes. Int J Lightweight Mater Manuf 2023;6:521–33. https://doi.org/10.1016/j.ijlmm.2023.04.001.

[16] Mahta M, Emamy M, Cao X, Campbell J. Overview of β-Al_5FeSi phase in Al-Si alloys. Materials Science Research Trends 2008:251–71.

[17] Park DS, Nam SW. Effects of manganese dispersoid on the mechanical properties in Al-Zn-Mg alloys. J Mater Sci 1995;30:1313–20. https://doi.org/10.1007/BF00356137.

[18] Zhang X, Le Q, Zhao D, Jiang Y, Wang Y, Wang T, et al. Research status and prospect of grain refinement in aluminum alloy. J Mater Res Technol 2025;34:1880–93. https://doi.org/10.1016/j.jmrt.2024.12.205.

[19] Zhang L, Jiang H, He J, Zhao J. Improved grain refinement in aluminium alloys by re-precipitated TiB2 particles. Mater Lett 2022;312:131657. https://doi.org/10.1016/j.matlet.2022.131657.

[20] Trujillo-Tadeo JJ, Arruebarrena G, Dorantes-Rosales HJ, Bilbao Y, Vicario I, Guraya T, et al. Design and characterization of a novel lightweight multicomponent alloy Al58Zn28Mg6Si8. J Mater Res Technol 2023;27:3751–60. https://doi.org/10.1016/j.jmrt.2023.10.102.

[21] Biswas P, Paliwal M, Mondal MK. Thermochemical behaviour, solidification, thermal stability and oxidation of Al-Mg2Si composites: an experimental and thermodynamic study. Mater Today Commun 2023;35:105913. https://doi.org/10.1016/j.mtcomm.2023.105913.

[22] Yuan GY, Liu ZL, Wang QD, Ding WJ. Microstructure refinement of Mg–Al–Zn–Si alloys. Mater Lett 2002;56:53–8. https://doi.org/10.1016/S0167-577X(02)00417-2.

[23] Nam KY, Song DH, Lee CW, Lee SW, Park YH, Cho KM, et al. Modification of Mg2Si morphology in As-Cast mg-al-si alloys with strontium and antimony. Mater Sci Forum 2006;510–511:238–41. https://doi.org/10.4028/www.scientific.net/MSF.510-511.238.

[24] Wang K-Y, Zhao R-D, Wu F-F, Wu X-F, Chen M-H, Xiang J, et al. Improving microstructure and mechanical properties of hypoeutectic Al-Mg2Si alloy by Gd addition. J Alloys Compd 2020;813:152178. https://doi.org/10.1016/j.jallcom.2019.152178.

[25] Wu X-F, Wang K-Y, Wu F-F, Zhao R-D, Chen M-H, Xiang J, et al. Simultaneous grain refinement and eutectic Mg2Si modification in hypoeutectic Al-11Mg2Si alloys by Sc addition. J Alloys Compd 2019;791:402–10. https://doi.org/10.1016/j.jallcom.2019.03.326.

[26] Moussa ME, Waly MA, El-Sheikh AM. Combined effect of high-intensity ultrasonic treatment and Ca addition on modification of primary Mg 2 Si and wear resistance in hypereutectic Mg–Si alloys. J Alloys Compd 2014;615:576–81. https://doi.org/10.1016/j.jallcom.2014.06.154.

[27] Chen K, Li ZQ, Liu JS, Yang JN, Sun YD, Bian SG. The effect of Ba addition on microstructure of in situ synthesized Mg2Si/Mg–Zn–Si composites. J Alloys Compd 2009;487:293–7. https://doi.org/10.1016/j.jallcom.2009.07.111.

[28] Qin QD, Zhao YG, Zhou W, Cong PJ. Effect of phosphorus on microstructure and growth manner of primary Mg2Si crystal in Mg2Si/Al composite. Mater Sci Eng, A 2007;447:186–91. https://doi.org/10.1016/j.msea.2006.10.076.

[29] Wang H, Liu F, Chen L, Zha M, Liu G, Jiang Q. The effect of Sb addition on microstructures and tensile properties of extruded Al–20Mg2Si–4Cu alloy. Mater Sci Eng, A 2016;657:331–8. https://doi.org/10.1016/j.msea.2016.01.063.

[30] Prach O, Horník J, Mykhalenkov K. Effect of the addition of Li on the structure and mechanical properties of hypoeutectic Al-Mg_2Si alloys. Acta Polytechnica 2015;55:253. https://doi.org/10.14311/AP.2015.55.0253.

[31] Li C, Wang C, Ju H, Xue X-N, Zha M, Wang H-Y. Prediction of modified morphology for primary Mg2Si induced by trace-element adsorption: a first-principles study. Materialia 2020;14:100875. https://doi.org/10.1016/j.mtla.2020.100875.

[32] Jafari Nodooshan HR, Liu W, Wu G, Bahrami A, Pech-Canul MI, Emamy M. Mechanical and tribological characterization of Al-Mg2Si composites after yttrium addition and heat treatment. J Mater Eng Perform 2014;23:1146–56. https://doi.org/10.1007/s11665-014-0900-4.

[33] Kapranos P, Carney C, Pola A, Jolly M. Advanced casting methodologies. Comprehensive Materials Processing 2014:39–67. https://doi.org/10.1016/B978-0-08-096532-1.00539-2.
[34] Samat S, Omar MZ, Baghdadi AH, Mohamed IF, Aziz AM. Mechanical properties and microstructures of a modified Al–Si–Cu alloy prepared by thixoforming process for automotive connecting rods. J Mater Res Technol 2021;10:1086–102. https://doi.org/10.1016/j.jmrt.2020.12.085.
[35] Li R, Liu L, Zhang L, Sun J, Shi Y, Yu B. Effect of squeeze casting on microstructure and mechanical properties of hypereutectic Al-xSi alloys. J Mater Sci Technol 2017;33:404–10. https://doi.org/10.1016/j.jmst.2017.02.004.
[36] Ma Z, Zhang H, Song W, Wu X, Jia L, Zhang H. Pressure-driven mold filling model of aluminum alloy melt/semi-solid slurry based on rheological behavior. J Mater Sci Technol 2020;39:14–21. https://doi.org/10.1016/j.jmst.2019.07.048.
[37] Qi M, Li J, Kang Y. Correlation between segregation behavior and wall thickness in a rheological high pressure die-casting AC46000 aluminum alloy. J Mater Res Technol 2019;8:3565–79. https://doi.org/10.1016/j.jmrt.2019.03.016.
[38] Sajjad M, Agirre J, Plata G, Lozares J, Mendiguren J. Characterization of friction coefficient at near solidus forming (NSF) conditions using T-shape compression test. J Manuf Process 2024;124:1259–72. https://doi.org/10.1016/j.jmapro.2024.07.009.
[39] Slater C, Plata G, Sánchez A, Lozares J, Hurtado I. A novel forming technique to coforge bimetal components into complex geometries. Manuf Lett 2020;26:21–4. https://doi.org/10.1016/j.mfglet.2020.09.006.
[40] Plata G, Lozares J, Sánchez A, Hurtado I, Slater C. Preliminary study on the capability of the novel near solidus forming (NSF) technology to manufacture complex steel components. Materials 2020;13:4682. https://doi.org/10.3390/ma13204682.
[41] Lozares J, Plata G, Hurtado I, Sánchez A, Loizaga I. Near solidus forming (NSF): semi-solid steel forming at high solid content to obtain As-Forged properties. Metals 2020;10:198. https://doi.org/10.3390/met10020198.
[42] Zhang Y, Zhou J, Yin Y, Ji X, Shen X, Guo Z. Study on the solutal convection during dendrite growth of superalloy under directional solidification condition. J Mater Res Technol 2023;23:3916–27. https://doi.org/10.1016/j.jmrt.2023.02.042.
[43] Zhang S, Xu Z, Wang Z. Numerical modeling and simulation of water cooling-controlled solidification for aluminum alloy investment casting. Int J Adv Manuf Technol 2017;91:763–70. https://doi.org/10.1007/s00170-016-9808-5.
[44] Xu J, Kang J, Zheng L, Mao W, Wang J. Numerical simulation of the directional solidification process with multi-shell mold being gradually immersed in water. J Mater Res Technol 2022;19:2705–16. https://doi.org/10.1016/j.jmrt.2022.06.037.
[45] Wang Y, Liu X, Dong D, Zhu D, Ding H, Chen R, et al. Temperature-dependent mechanical properties and fracture behavior of directionally solidified Ti47Al2Cr2Nb alloy. J Mater Res Technol 2023;25:570–80. https://doi.org/10.1016/j.jmrt.2023.05.182.
[46] Peng P, Lu L, Zheng W, Wang J, Zhou S. Thermosolutal convection-induced freckle formation in steady and unsteady directional solidification: analysis in Sn-Ni peritectic alloy. J Alloys Compd 2021;872:159558. https://doi.org/10.1016/j.jallcom.2021.159558.
[47] Ye C, Jia L, Jin Z, Wang Y, Zhang H. Directional solidification of hypereutectic Nb-Si-Ti alloy: influence of drawing velocity change on microstructures. J Alloys Compd 2020;844:156123. https://doi.org/10.1016/j.jallcom.2020.156123.
[48] Xu X, Hao Y, Wu Q, Dong R, Zhao Y, Hou H. Microstructure refinement mechanisms in undercooled solidification of binary and ternary nickel based alloys. J Mater Res Technol 2023;24:737–58. https://doi.org/10.1016/j.jmrt.2023.03.004.
[49] Wang H, Long H, Sun M, Yang G, Wei H, Mao S, et al. Effect of directional solidification methods on solid solution window in Ni-based single-crystal superalloy. J Mater Res Technol 2023;24:8307–19. https://doi.org/10.1016/j.jmrt.2023.05.089.
[50] Bale CW, Bélisle E, Chartrand P, Decterov SA, Eriksson G, Gheribi AE, et al. FactSage thermochemical software and databases, 2010–2016. Calphad 2016;54:35–53. https://doi.org/10.1016/j.calphad.2016.05.002.
[51] Elsayed FR, Hort N, Salgado Ordorica MA, Kainer KU. Magnesium permanent mold castings optimization. Mater Sci Forum 2011;690:65–8. https://doi.org/10.4028/www.scientific.net/MSF.690.65.
[52] Wang S, Zhao Y, Hou H, Wen Z, Zhang P, Liang J. Effect of anti-site point defects on the mechanical and thermodynamic properties of MgZn2, MgCu2 laves phases: a first-principle study. J Solid State Chem 2018;263:18–23. https://doi.org/10.1016/j.jssc.2018.04.001.
[53] Liu CT, Zhu JH, Brady MP, McKamey CG, Pike LM. Physical metallurgy and mechanical properties of transition-metal laves phase alloys. Intermetallics 2000;8:1119–29. https://doi.org/10.1016/S0966-9795(00)00109-6.
[54] Scudino S, Donnadieu P, Surreddi KB, Nikolowski K, Stoica M, Eckert J. Microstructure and mechanical properties of laves phase-reinforced Fe–Zr–Cr alloys. Intermetallics 2009;17:532–9. https://doi.org/10.1016/j.intermet.2009.01.007.
[55] Zhang L, Chen S, Li Q, Chang G. Formation mechanism and conditions of fine primary silicon being uniformly distributed on single αAl matrix in Al-Si alloys. Mater Des 2020;193:108853. https://doi.org/10.1016/j.matdes.2020.108853.
[56] Chandra K, Kain V. Brittle failure of hypereutectic Al–Si alloy component. J Fail Anal Prev 2015;15:679–85. https://doi.org/10.1007/s11668-015-9996-6.
[57] Joseph S, Tewari A, Kumar S. The fracture characteristics of a near eutectic Al-Si based alloy under compression. Metall Mater Trans 2013;44:2358–68. https://doi.org/10.1007/s11661-012-1580-z.
[58] Xu CL, Jiang QC. Morphologies of primary silicon in hypereutectic Al–Si alloys with melt overheating temperature and cooling rate. Mater Sci Eng, A 2006;437:451–5. https://doi.org/10.1016/j.msea.2006.07.088.
[59] Xu CL, Jiang QC, Yang YF, Wang HY, Wang JG. Effect of Nd on primary silicon and eutectic silicon in hypereutectic Al–Si alloy. J Alloys Compd 2006;422:L1–4. https://doi.org/10.1016/j.jallcom.2005.03.128.
[60] Yang M, Pan F, Shen J, Bai L. Comparison of Sb and Sr on modification and refinement of Mg2Si phase in AZ61-0.7Si magnesium alloy. Trans Nonferrous Metals Soc China 2009;19:287–92. https://doi.org/10.1016/S1003-6326(08)60266-6.
[61] Dong Y, Xiao P, Gao Y, Zhao Q, Yang H. Microstructure refinement and mechanical properties of eutectic Mg2Si reinforced Mg matrix composites containing Sr element. J Mater Res Technol 2022;17:2614–23. https://doi.org/10.1016/j.jmrt.2022.02.035.
[62] Bilbao Y, Trujillo JJ, Vicario I, Arruebarrena G, Hurtado I, Guraya T. X-ray thermo-diffraction study of the aluminum-based multicomponent alloy Al58Zn28Si8Mg6. Materials 2022;15:5056. https://doi.org/10.3390/ma15145056.
[63] Ke G, Yue R, Huang H, Kang B, Zeng H, Yuan G. Effects of Sr addition on microstructure, mechanical properties and in vitro degradation behavior of as-extruded Zn−Sr binary alloys. Trans Nonferrous Metals Soc China 2020;30:1873–83. https://doi.org/10.1016/S1003-6326(20)65346-8.
[64] Gutiérrez-Menchaca J, Torres-Torres D, Garay-Tapia AM. Microstructural, mechanical and thermodynamic study of the as-cast Zn–Al–Sr alloys at high Sr content. J Alloys Compd 2020;829:154511. https://doi.org/10.1016/j.jallcom.2020.154511.
[65] Liu G, Liu L, Liu X, Wang Z, Han Z, Zhang G, et al. Microstructure and mechanical properties of Al0.7CoCrFeNi high-entropy-alloy prepared by directional solidification. Intermetallics 2018;93:93–100. https://doi.org/10.1016/j.intermet.2017.11.019.
[66] Zheng H, Chen R, Qin G, Li X, Su Y, Ding H, et al. Microstructure evolution, Cu segregation and tensile properties of CoCrFeNiCu high entropy alloy during directional solidification. J Mater Sci Technol 2020;38:19–27. https://doi.org/10.1016/j.jmst.2019.08.019.
[67] Lukasz Rogal, Adrianna Kania, Katarzyna Berent, Karol Janus, Lidia Lityńska-Dobrzyńska. Microstructure and mechanical properties of Mg–Zn–RE–Zr alloy after thixoforming. J Mater Res Technol 2019;8:1121–31. https://doi.org/10.1016/j.jmrt.2018.09.002.
[68] Asadikiya M, Zhang Y, Wang L, Apelian D, Zhong Y. Design of ternary high-entropy aluminum alloys (HEAls). J Alloys Compd 2022;891:161836. https://doi.org/10.1016/j.jallcom.2021.161836.
[69] Zenk CH, Neumeier S, Stone HJ, Göken M. Mechanical properties and lattice misfit of γ/γ' strengthened Co-base superalloys in the Co–W–Al–Ti quaternary system. Intermetallics 2014;55:28–39. https://doi.org/10.1016/j.intermet.2014.07.006.
[70] Souza FA, Costa MO, Magno IA, Nascimento JM, Silva AP, Costa TS, et al. Investigation on microstructural and microhardness evolution in as-cast and T6/heat-treated samples of a horizontally solidified AlSiCu alloy. J Mater Res Technol 2019;8:5046–52. https://doi.org/10.1016/j.jmrt.2019.06.054.
[71] Hall EO. The deformation and ageing of mild steel: III discussion of results. Proc Phys Soc B 1951;64:747–53. https://doi.org/10.1088/0370-1301/64/9/303.
[72] Fleischer RL. Substitutional solution hardening. Acta Metall 1963;11:203–9. https://doi.org/10.1016/0001-6160(63)90213-X.
[73] Labusch R. A statistical theory of solid solution hardening. Phys Status Solidi 1970;41:659–69. https://doi.org/10.1002/pssb.19700410221.
[74] Liao Y-C, Chen P-S, Li C-H, Tsai P-H, Jang J, Hsieh K-C, et al. Development of novel lightweight dual-phase Al-Ti-Cr-Mn-V medium-entropy alloys with high strength and ductility. Entropy 2020;22:74. https://doi.org/10.3390/e22010074.
[75] Li R, Gao JC, Fan K. Microstructure and mechanical properties of MgMnAlZnCu high entropy alloy cooling in three conditions. Mater Sci Forum 2011;686:235–41. https://doi.org/10.4028/www.scientific.net/MSF.686.235.
[76] Han M, Wu Y, Zong X, Shen Y, Zhang F, Lou H, et al. Lightweight single-phase Al-based complex concentrated alloy with high specific strength. Nat Commun 2024;15:7102. https://doi.org/10.1038/s41467-024-51387-6.
[77] Liao Y-C, Chen P-S, Li C-H, Tsai P-H, Jang J, Hsieh K-C, et al. Development of novel lightweight dual-phase Al-Ti-Cr-Mn-V medium-entropy alloys with high strength and ductility. Entropy 2020;22:74. https://doi.org/10.3390/e22010074.
[78] Chen P-S, Liao Y-C, Lin Y-T, Tsai P-H, Jang JSC, Hsieh K-C, et al. Development of novel lightweight Al-Rich quinary medium-entropy alloys with high strength and ductility. Materials 2021;14:4223. https://doi.org/10.3390/ma14154223.
[79] Jia Y, Jia Y, Wu S, Ma X, Wang G. Novel ultralight-weight complex concentrated alloys with high strength. Materials 2019;12. https://doi.org/10.3390/ma12071136.
[80] Kumar A, Gupta M. An insight into evolution of light weight high entropy alloys: a review. Metals 2016;6. https://doi.org/10.3390/met6090199.

I am Juan José Trujillo Tadeo, a materials engineer specializing in lightweight alloys and the composition–process–microstructure–property nexus. During my doctoral work, I contributed to multiple projects spanning computational thermodynamics (CALPHAD), processing—casting, directional solidification, near-solidus forming, hot rolling, and extrusion—and advanced characterization (SEM-EDS, EBSD, XRD, nanoindentation), complemented by casting/forming simulations. I am currently a postdoctoral researcher at Hereon, where I study magnesium alloys, combining synchrotron diffraction (in-situ/ex-situ), DSC, and microscopy/EDS to track phase transformations and precipitation kinetics and their impact on corrosion, corrosion-fatigue, and mechanical strength within DFG-funded projects. In parallel, I have 8+ years of industrial experience as a mechanical integrity engineer in oil & gas, including Fitness-For-Service evaluations, finite element analysis (FEA), and technical training (pipeline analysis courses). Beyond Mg and Al systems, my portfolio includes high-temperature alloys and high-entropy alloys (HEAs).